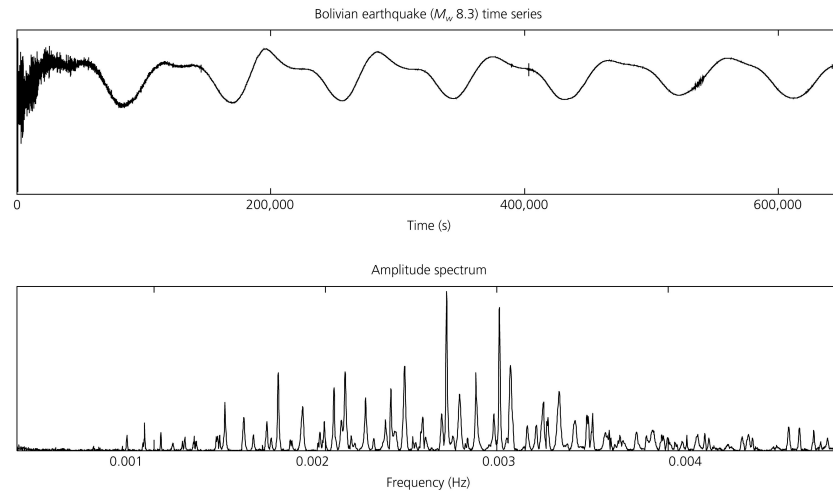


Earth & Planetary Sciences 327

Geophysical Time Series Analysis

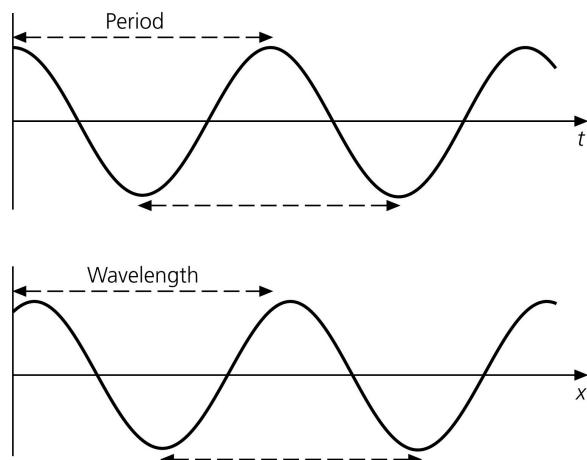
Figure 6.2-4: Amplitude spectra of a vertical-component seismogram from the great 1994 Bolivian earthquake.



1

QUANTITY	UNITS	
Velocity	distance/time	$v = \omega/k = f\lambda = \lambda/T$
Period	time	$T = 2\pi/\omega = 1/f = \lambda/v$
Angular Frequency	time^{-1}	$\omega = 2\pi/T = 2\pi f = kv$
Frequency	time^{-1}	$f = \omega/(2\pi) = 1/T = v/\lambda$
Wavelength	distance	$\lambda = 2\pi/k = v/f = vT$
Wavenumber	distance^{-1}	$k = 2\pi/\lambda = \omega/v = 2\pi f/v$

Figure 2.2-4: Harmonic wave, $u = A \cos(\omega t - kx)$.



2

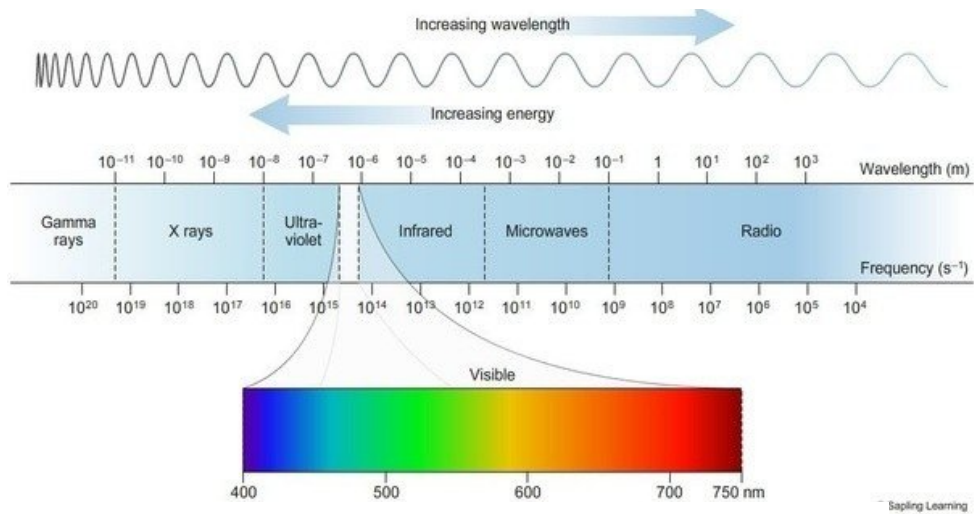
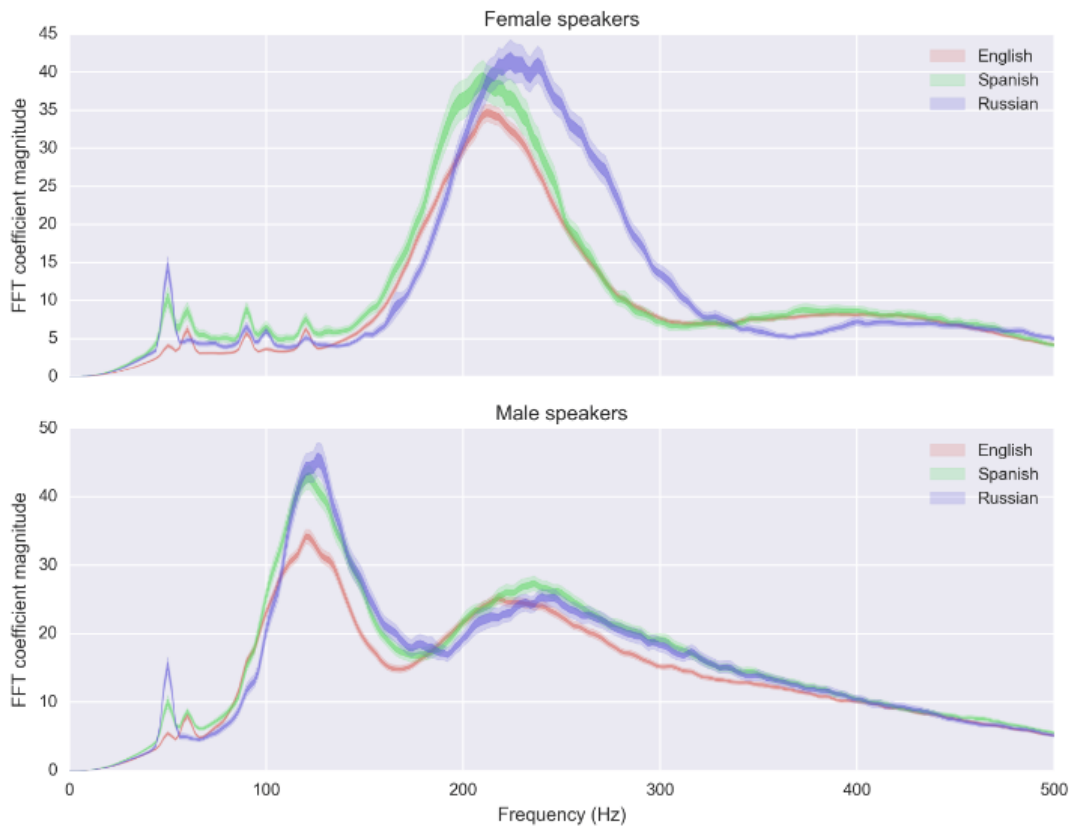
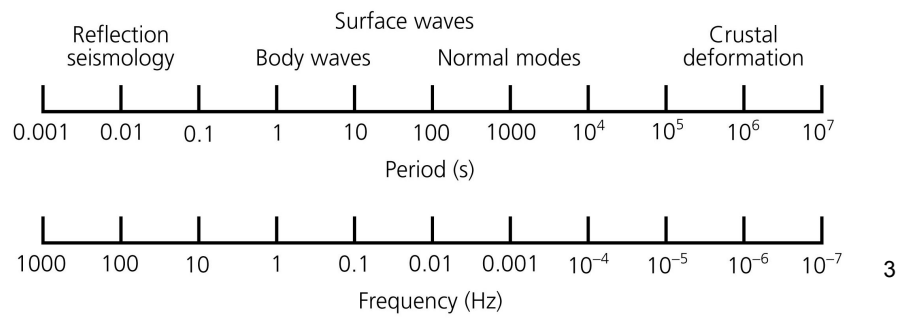


Figure 2.4-7: Seismic spectrum for various studies.





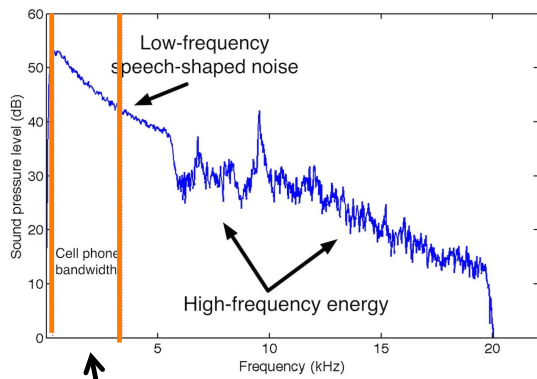
<https://www.matinee.co.uk/blog/difference-male-female-voice/>

5

The screenshot shows the NaturalReader website homepage. At the top left is the NaturalReader logo. To its right are navigation links: ONLINE, SOFTWARE, COMMERCIAL, and EXPLORE. Further right is a button labeled "Go To Online Reader". The main heading is "The Most Powerful Text to Speech Reader". Below this is the text "Try your own text and documents now!". At the bottom left are two buttons: "▶ Watch Video" and "Go To Online Reader".

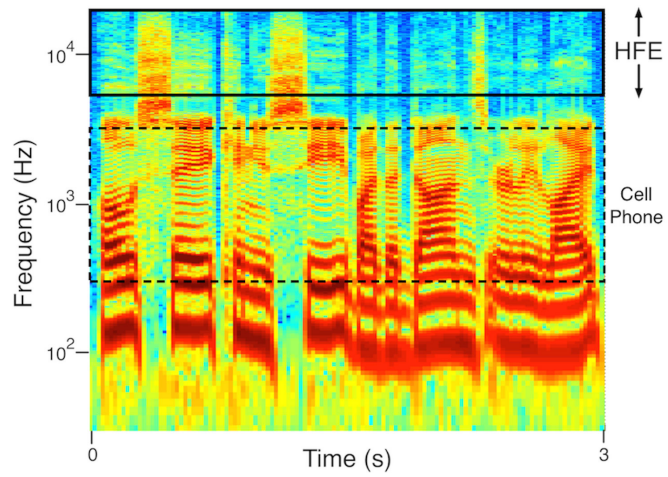
<https://www.naturalreaders.com/online/>

6



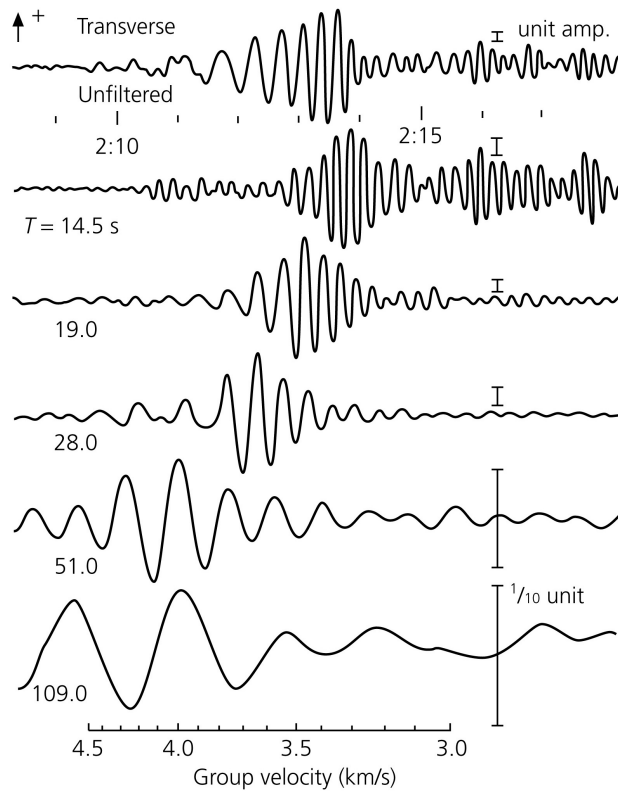
300 – 4300 Hz

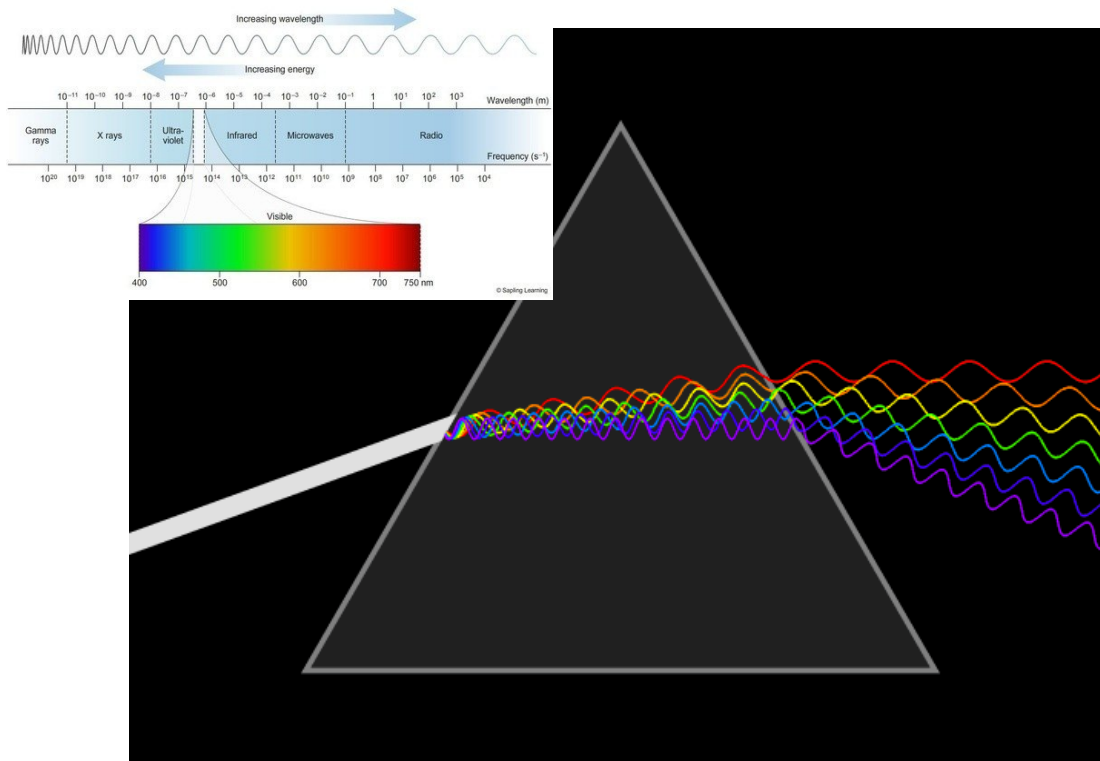
Spectrogram



<https://acoustics.org/hearing-voices-in-the-high-frequencies-what-your-cell-phone-isnt-telling-you-brian-b-monson/>

Figure 2.8-4: Example of Love wave group velocity dispersion through bandpass filtering.





9

http://load.wikimedia.org/wikipedia/commons/f/f5/Light_dispersion_conceptual_waves.gif

Figure 3.7-1: Regional effects of attenuation.

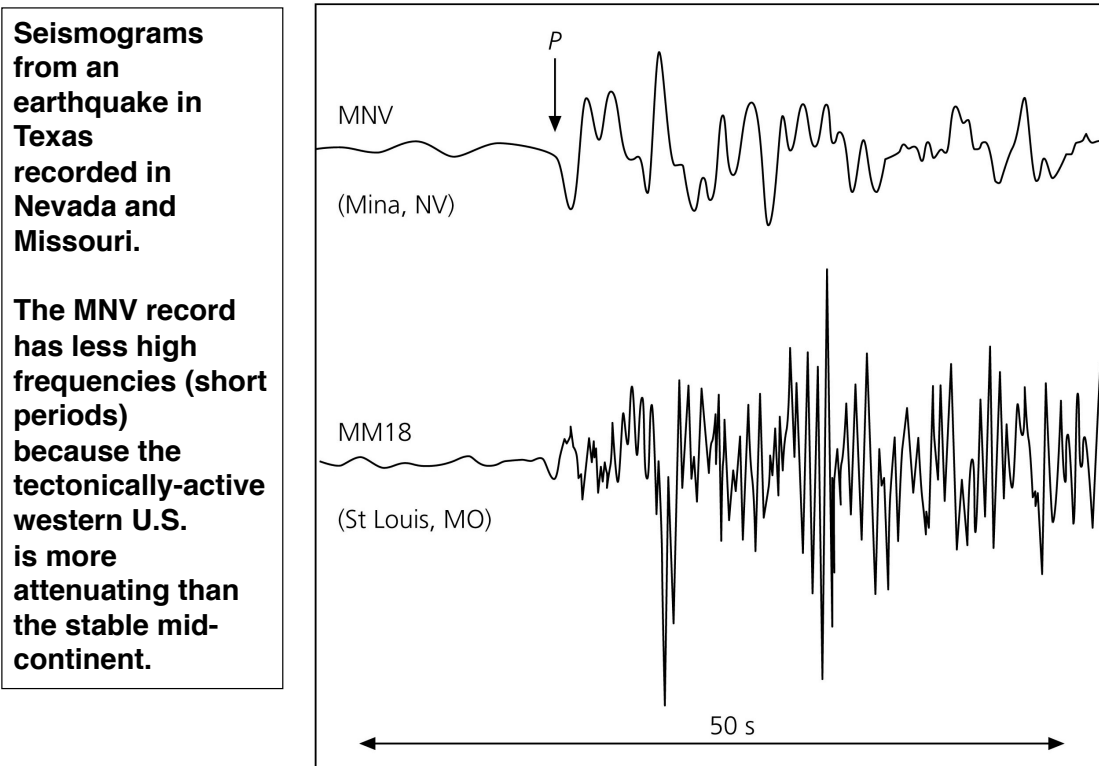
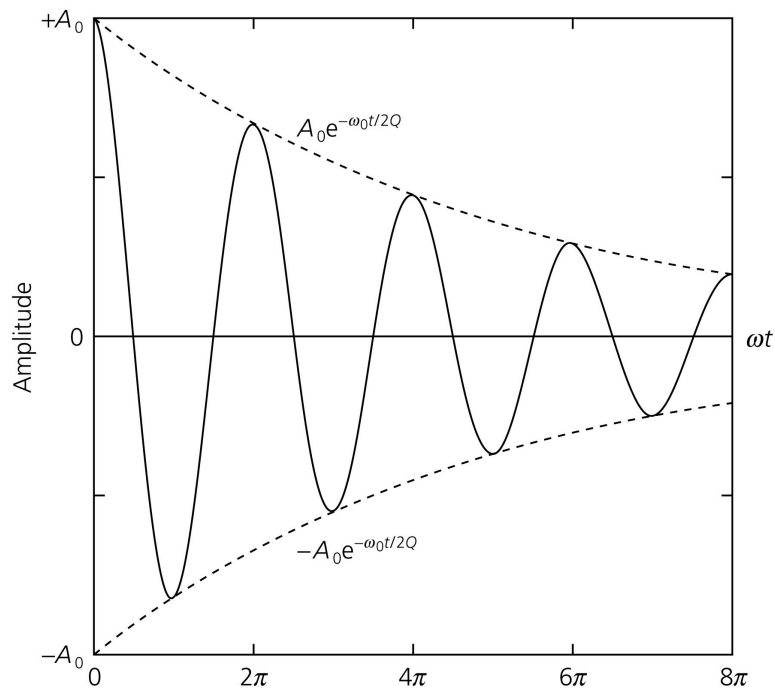
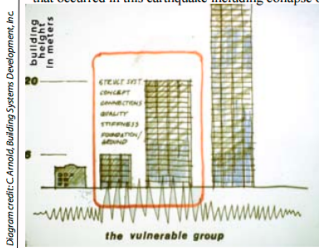


Figure 3.7-11: Wave amplitude for a damped harmonic oscillator.

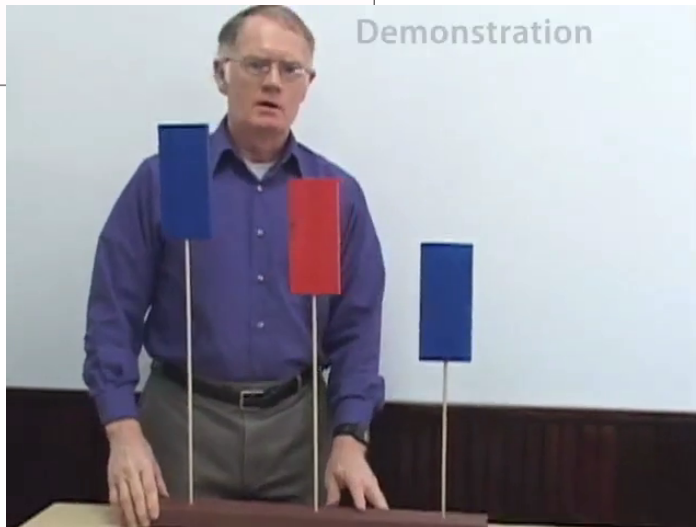


Tall and small stay up; medium fall: Mexico, 1985—10,000 die.

On September 19, 1985, a magnitude 8.1 earthquake occurred off the Pacific coast of Mexico. 350 km from the epicenter damage was concentrated in a 25 km² area of Mexico City. The underlying geology contributed to this unusual concentration of damage at a distance from the epicenter. An estimated 10,000 people were killed, and 50,000 were injured. In addition, 250,000 people lost their homes. The set of slides (link below), shows different types of damaged buildings and the major kinds of structural failure that occurred in this earthquake including collapse of top, middle and bottom floors and total building failure.



Interestingly, the short and tall buildings remained standing. Medium-height buildings were the most vulnerable structures in the September 19 earthquake. Of the buildings that either collapsed or incurred serious damage, about 60% were in the 6-15 story range. The resonance frequency of such buildings coincided with the frequency range amplified most frequently in the subsoils.



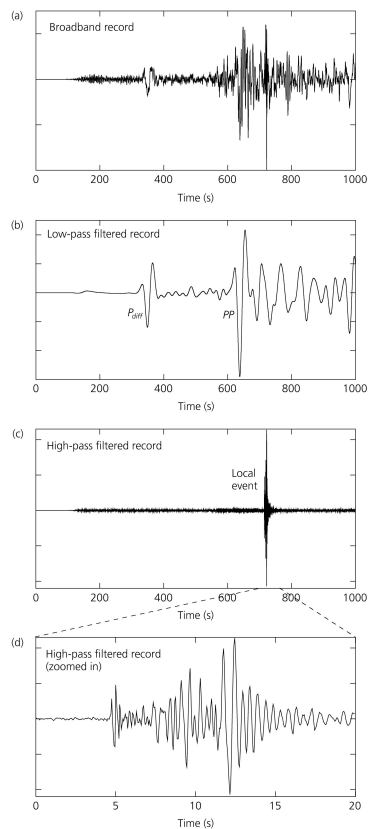
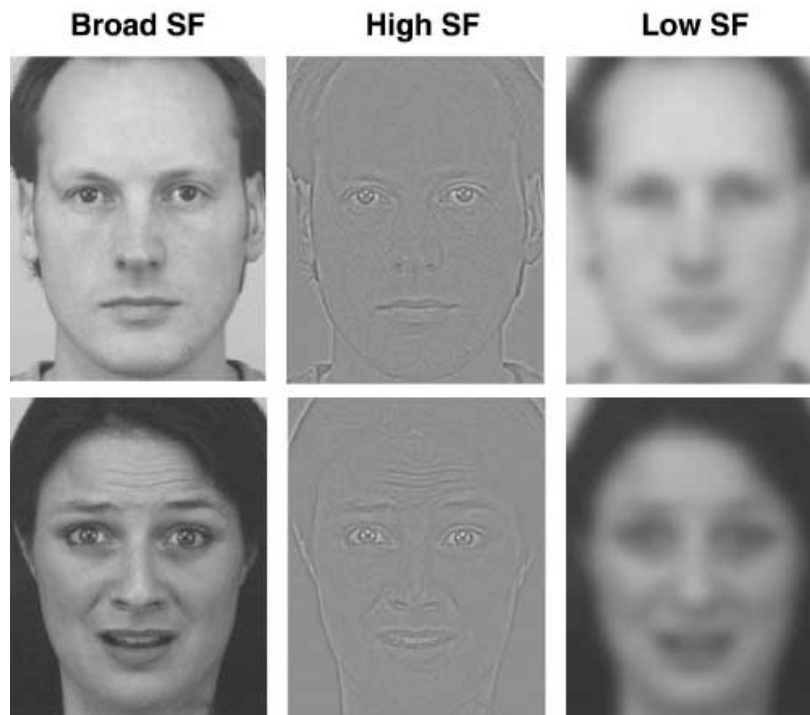
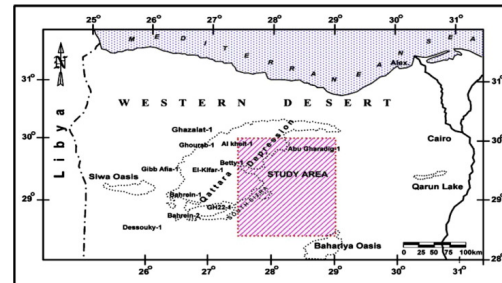
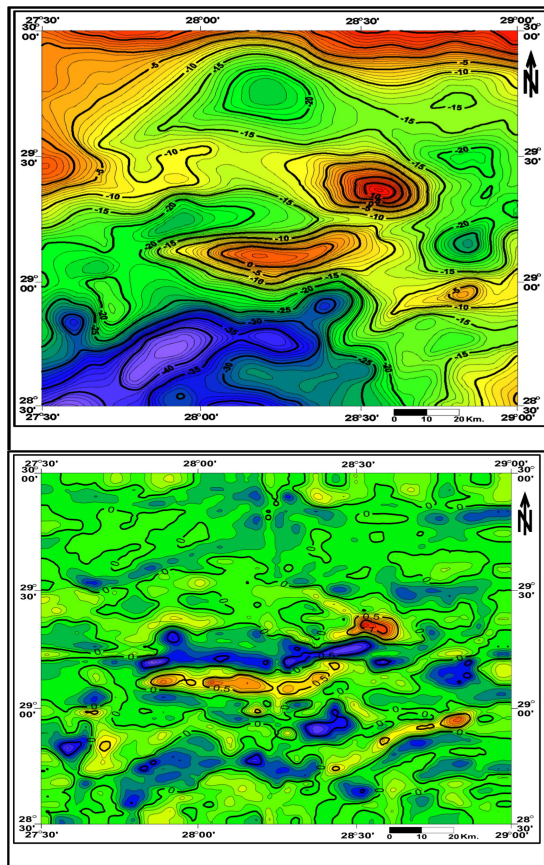


Figure 6.6-11

Using filters to enhance different frequencies in a seismogram and pick out a local earthquake signal from within a teleseismic earthquake record

13

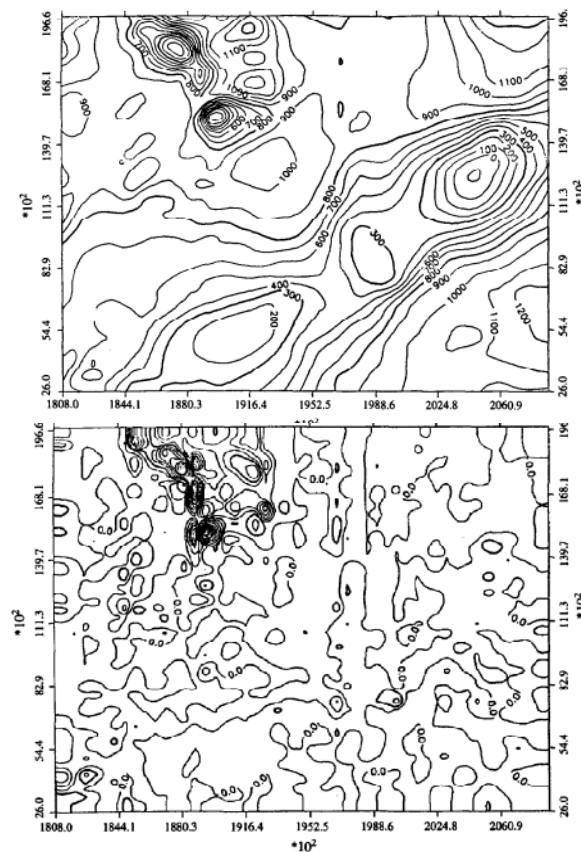




Bouguer gravity

High-pass filtered

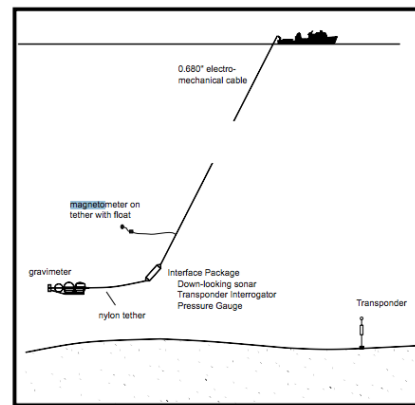
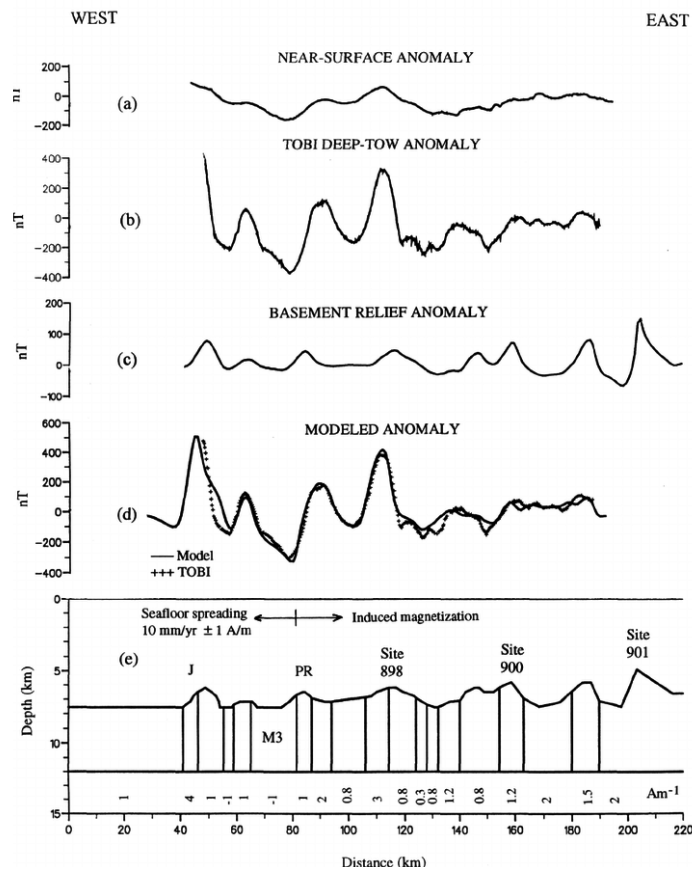
Zahra, H. S., & Oweis, H. T. (2016). Application of high-pass filtering techniques on gravity and magnetic data of the eastern Qattara Depression area, Western Desert, Egypt. *NRIAG Journal of Astronomy and Geophysics*, 5(1), 15 106-123.



Raw aeromagnetic

High-pass filtered

Cooper, G. R. J. (1997). GravMap and PFproc: software for filtering geophysical map data. *Computers & Geosciences*, 23(1), 91-101.



Gee, Jeffrey S. et al. "A deep tow magnetic survey of Middle Valley, Juan de Fuca Ridge." *Geochemistry, Geophysics, Geosystems* 2, (2001).

Geological and geophysical implications of deep-tow magnetometer observations near Sites 897, 898, 899, 900 and 901 on the west Iberia continental margin

Proceedings of the Ocean Drilling Program, Scientific Results, 149
Chapter: 43: Whitmarsh R.B. et al

12

Figure 6.2-1: Successive terms of a Fourier series.

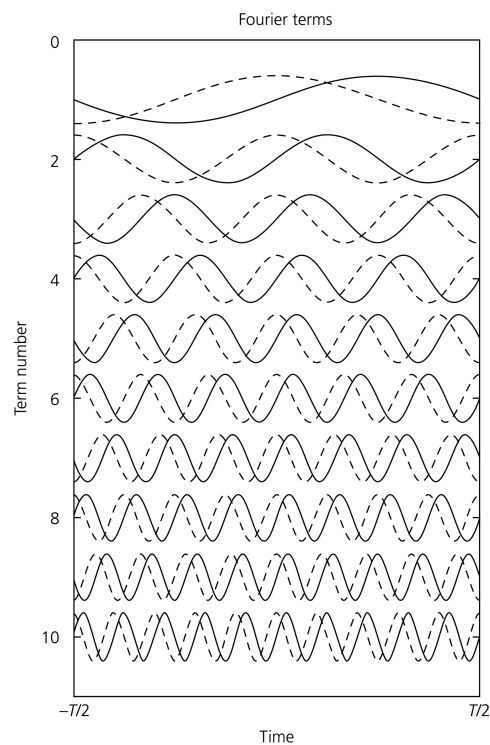
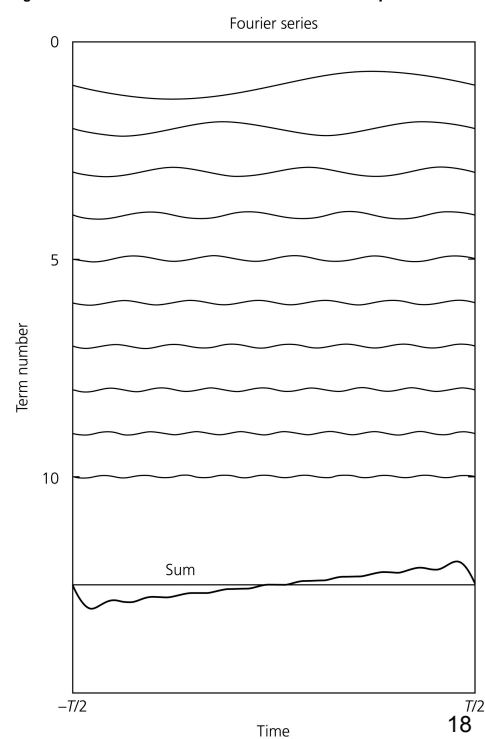
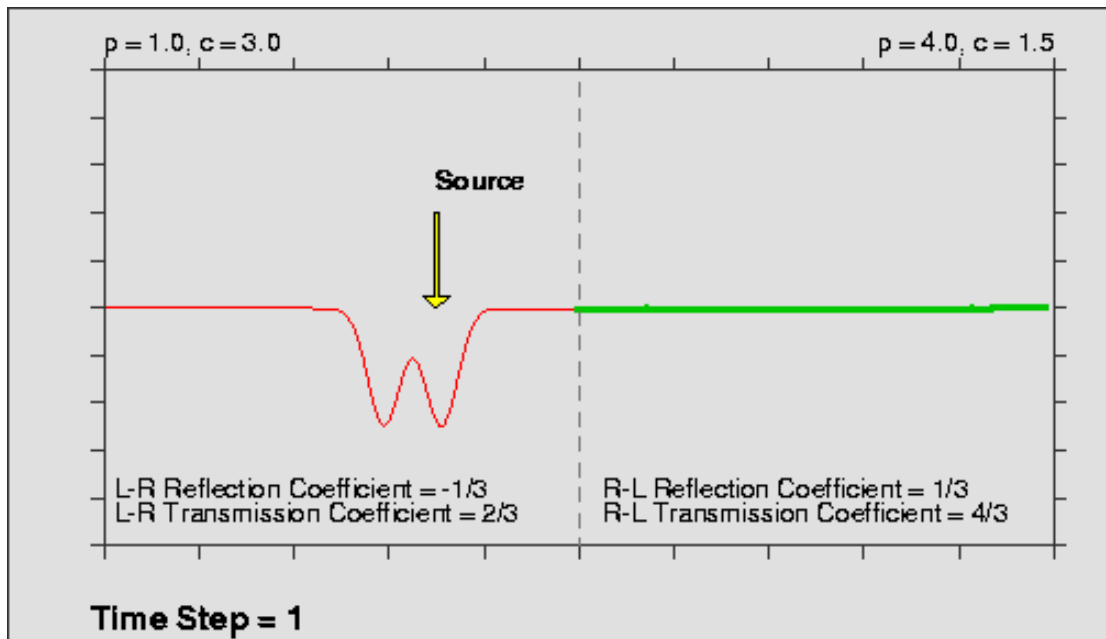


Figure 6.2-2: First ten terms of the Fourier series for a ramp function.





19

$$u(x, t) = \sum_{n=0}^{\infty} \sin(n\pi x_s/L) F(\omega_n) \sin(n\pi x/L) \cos(\omega_n t)$$

Figure 2.2-8: Waves on a string as a summation of modes.

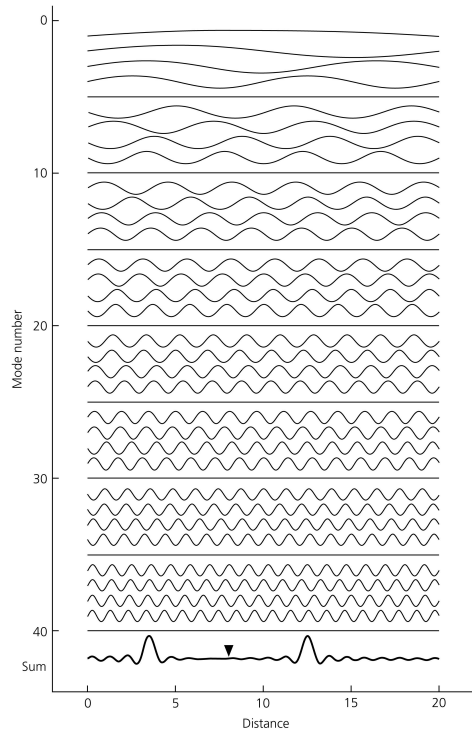
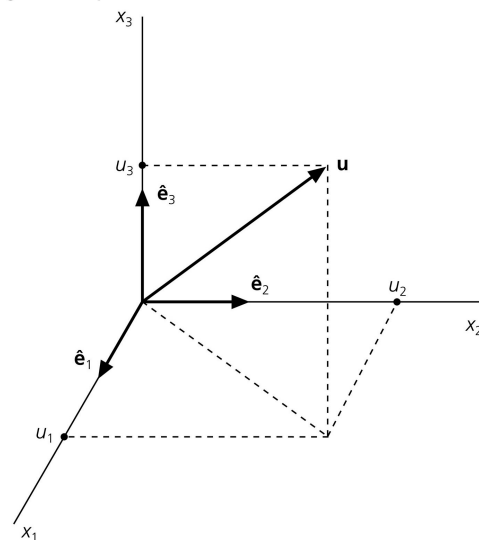
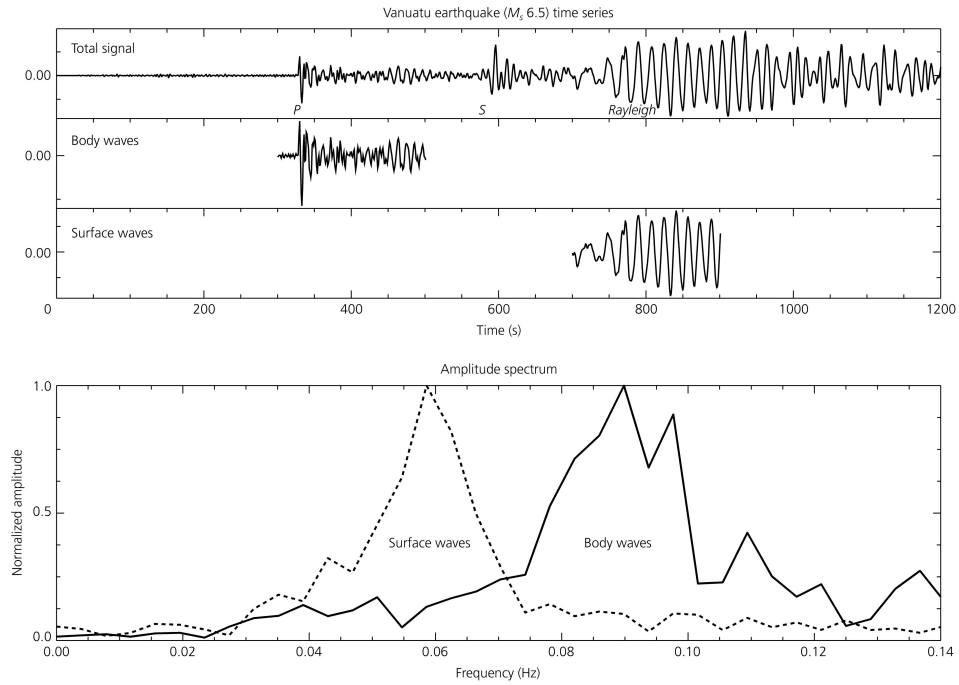


Figure A.3-1: Representation of a vector in Cartesian coordinates.



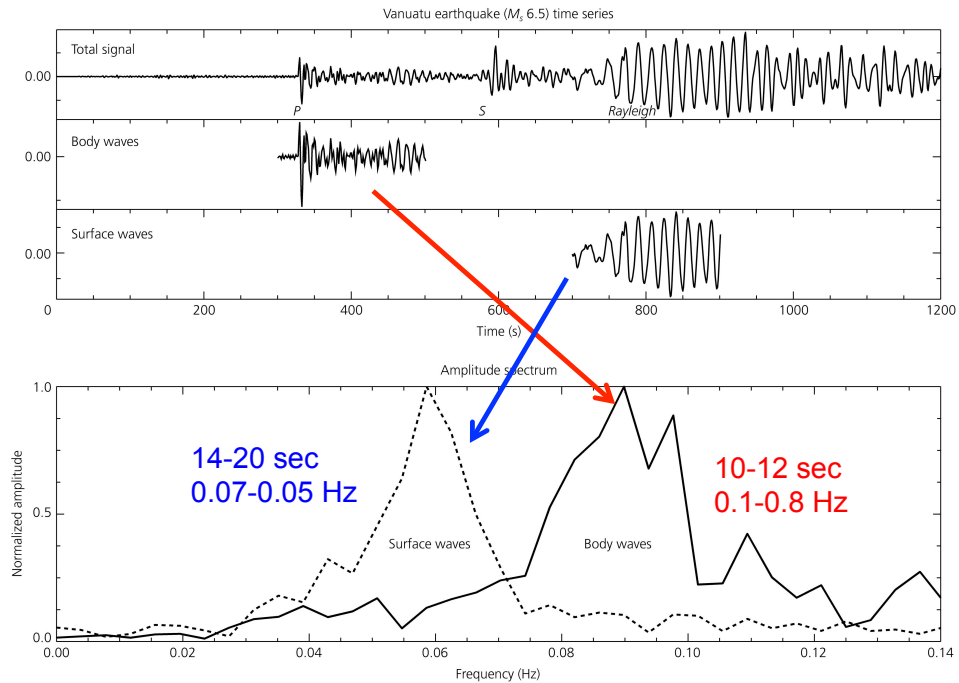
20

Figure 6.2-3: Amplitude spectra for the body and surface wave segments from a large earthquake.



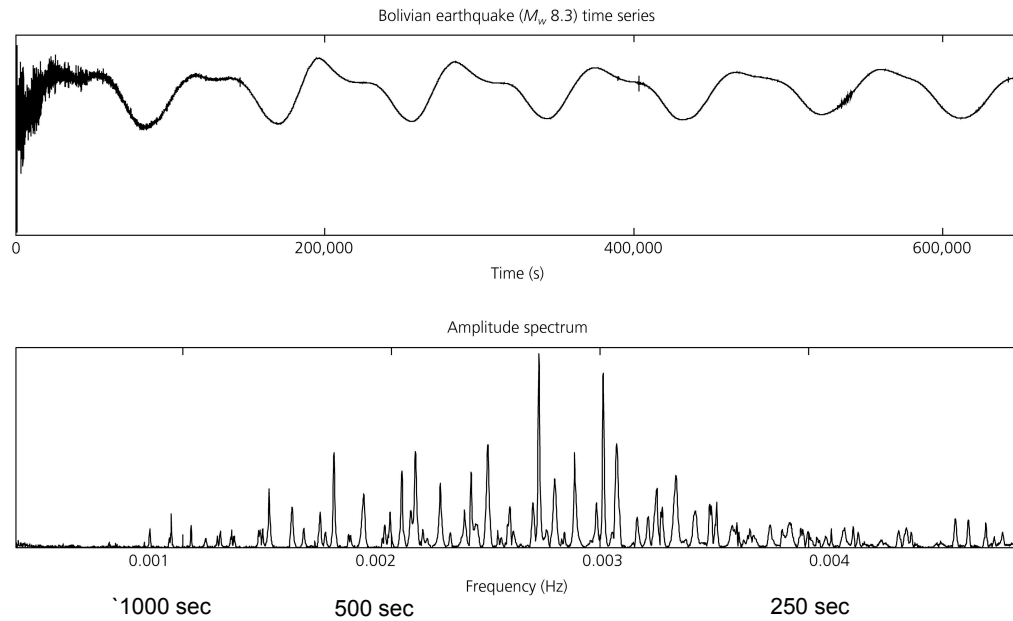
21

Figure 6.2-3: Amplitude spectra for the body and surface wave segments from a large earthquake.

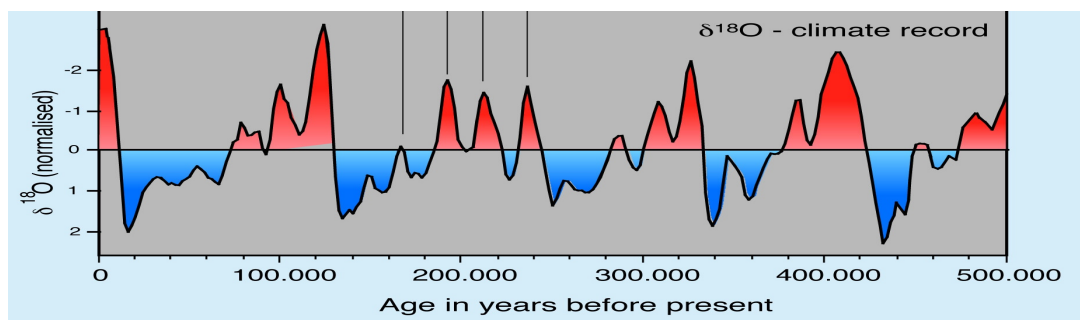
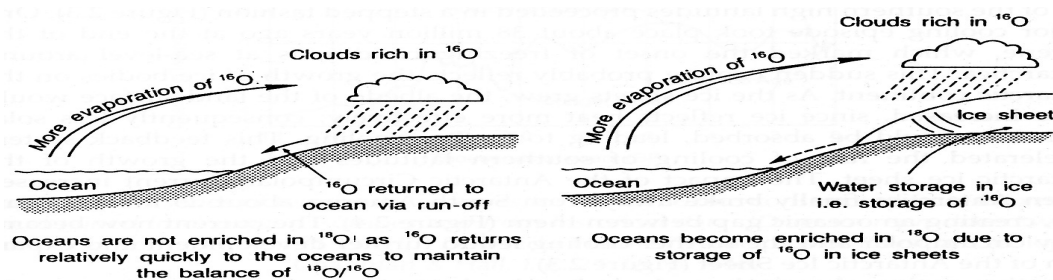


22

Figure 6.2-4: Amplitude spectra of a vertical-component seismogram from the great 1994 Bolivian earthquake.



23



24

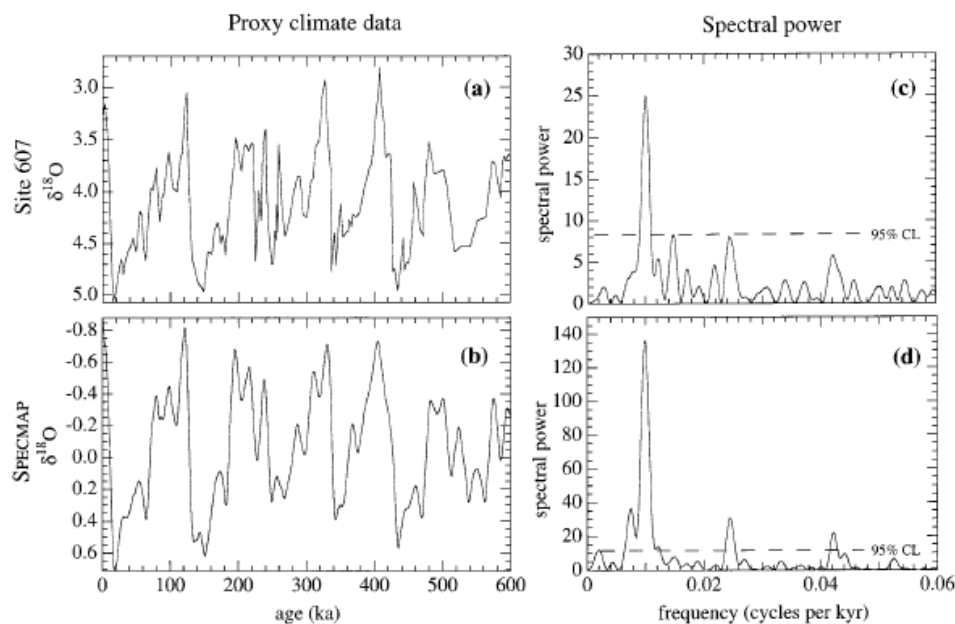
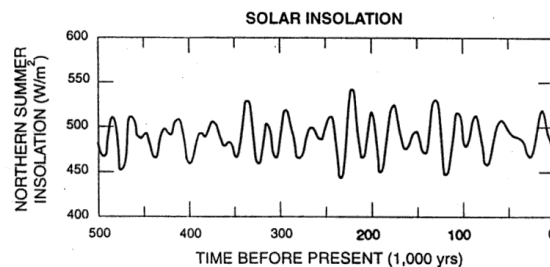
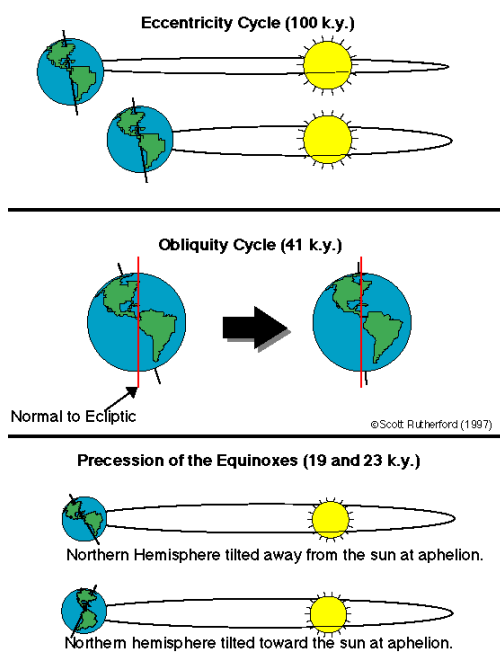


FIG. 1. $\delta^{18}\text{O}$ for past 800 kyr. (a) Data of site 607 from Ruddiman *et al.* (15). (b) Specmap stack of Imbrie *et al.* (16). (c) Spectral power of site 607. (d) Spectral power of Specmap. In the Milankovitch theory, the peak near 0.01 (100-kyr period) is attributed to eccentricity, the peak near 0.024 (41-kyr period) to obliquity, and the peak near 0.043 (23-kyr period) to precession.

25



Variations in insolation (in watts per square meter) determined from the variation in Earth's orbital elements (Barron, 1994, figure 13).

26

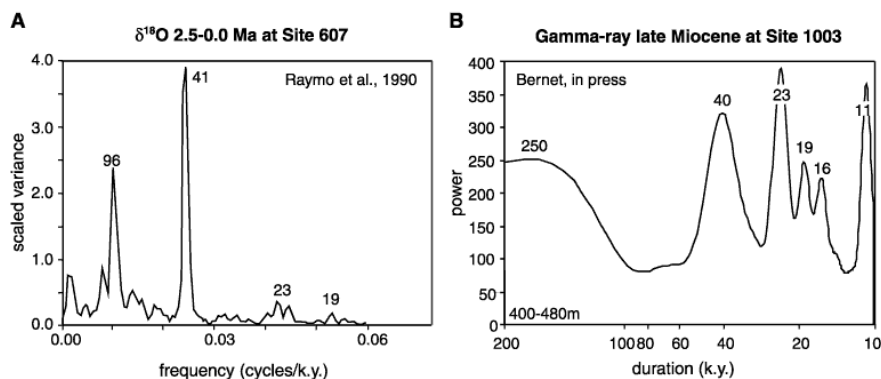


Figure 4. Two spectral analyses using the Blackman-Tukey method. A. ^{18}O spectrum of Site 607 shows that ^{18}O variations indicative for glaciations occur at the primary Milankovitch frequencies. Obliquity, however, is the dominant frequency (Raymo et al., 1990). B. Gamma-ray spectrum of Miocene marl/limestone alternations at Site 1003 produces frequencies at 40, 23, 19, 16, and 11 k.y. The strongest peak occurs at 23 k.y., indicating the dominance of orbital precession on these sedimentary cycles (Bernet, 2000).

http://www-odp.tamu.edu/publications/166_SR/chap_16/c16_f4.htm

27

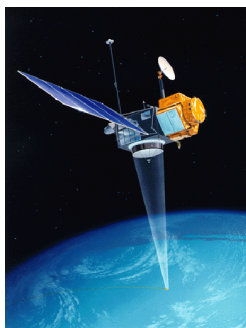


Figure 8: Amplitude and phase of the annual cycle of elevation in TOPEX/POSEIDON data estimated from 4 years of data. The amplitude is in centimeters, the phase in degrees measured from January 1. Areas of extreme air/sea exchanges produce large variations in elevation due to anomalies in heat added or removed by the atmosphere. The structures apparent in the quieter oceanic interior are related to wavelike motions.

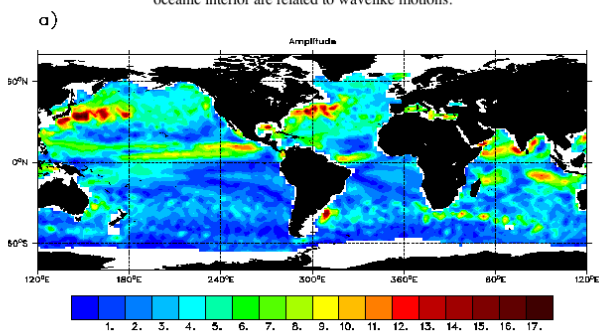
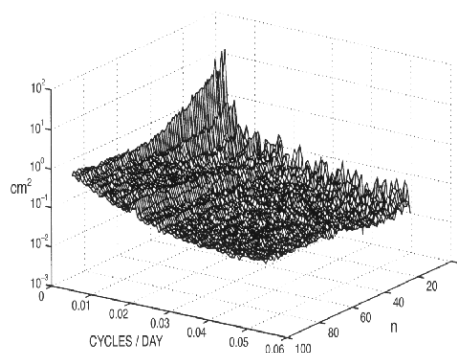


Figure 11: Frequency-wavenumber sea surface height spectrum computed from a spherical harmonic fit as described in Wunsch and Stammer, 1995, but from four years of data. Wavenumbers are actually in terms of spherical harmonic order n , for which the wavelengths are approximately 40,000 km/n.



28

FOURIER TRANSFORM

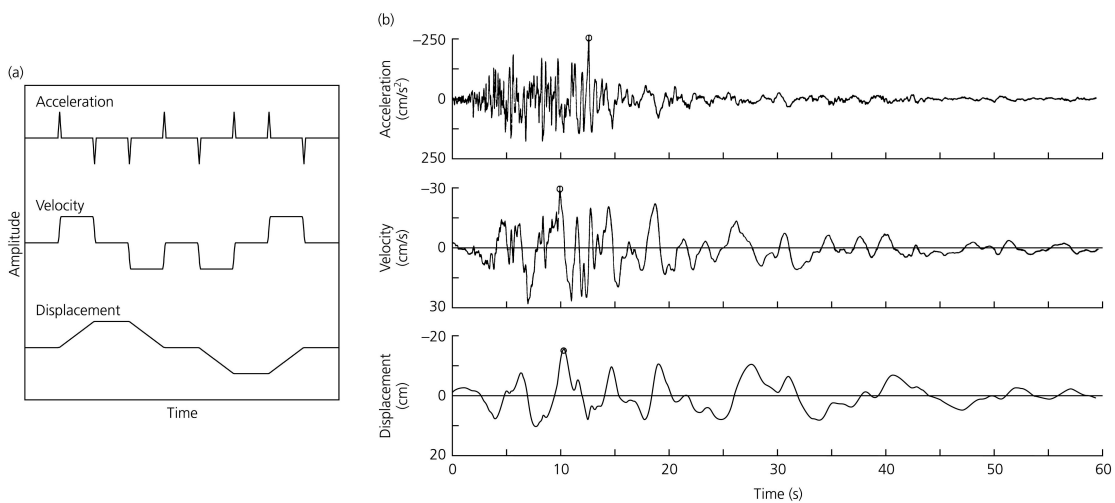
$$F(\omega) = \int_{-\infty}^{\infty} f(t)e^{-i\omega t} dt.$$

INVERSE FOURIER TRANSFORM

$$f(t) = \frac{1}{2\pi} \int_{-\infty}^{\infty} F(\omega)e^{i\omega t} d\omega,$$

29

Figure 6.6-14: Relation between displacement, velocity, and acceleration in the time domain.



30

SPECTRAL CORNER FREQUENCY APPROACH

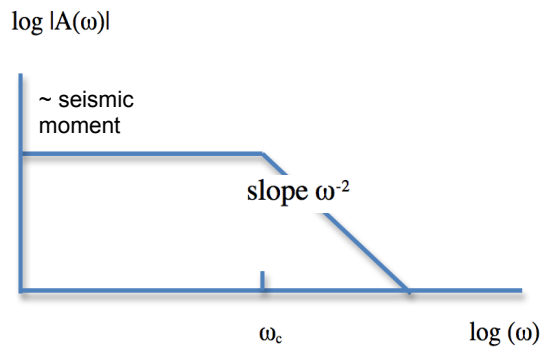
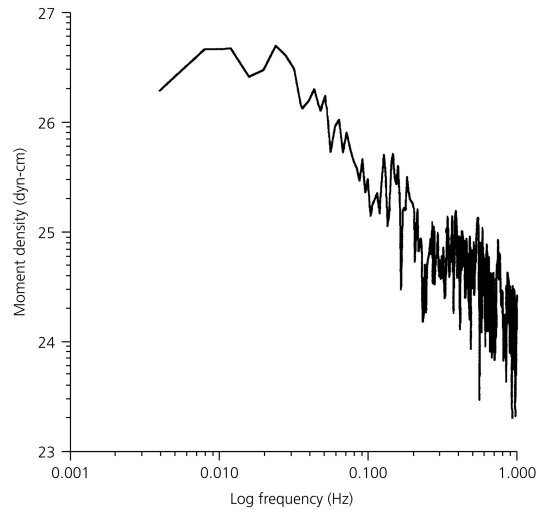
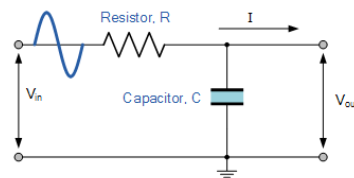


Figure 4.6-8: Sample amplitude spectrum, for the 1995 Chiapas, Mexico, earthquake.



The low frequency portion of the spectrum yields a moment of 5.2×10^{26} dyn-cm, in reasonable agreement with other studies which found 4.6 and 7.1×10^{26} dyn-cm

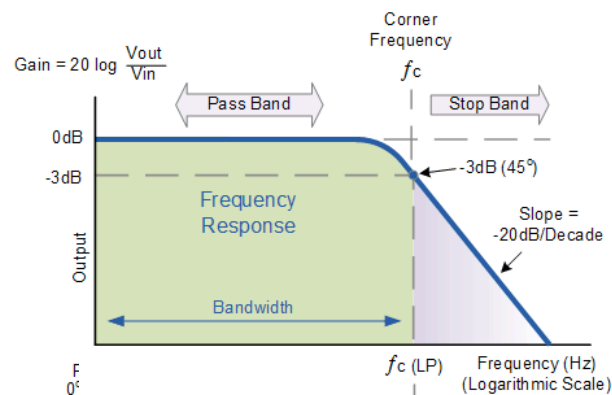
RC Low Pass Filter Circuit



Cut-off Frequency and Phase Shift

$$f_c = \frac{1}{2\pi RC} = 720 \text{ Hz}$$

Frequency Response of a 1st-order Low Pass Filter



https://www.electronicstutorials.ws/filter/filter_2.html

Figure 6.2-5: Two definitions of a delta function at $t = t_0$.

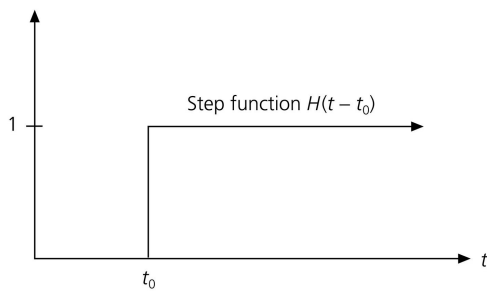
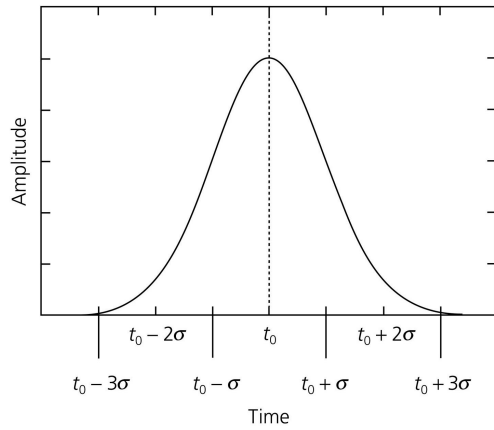


Figure 6.2-6: Amplitude and phase spectra of the Fourier transform of a delta function.

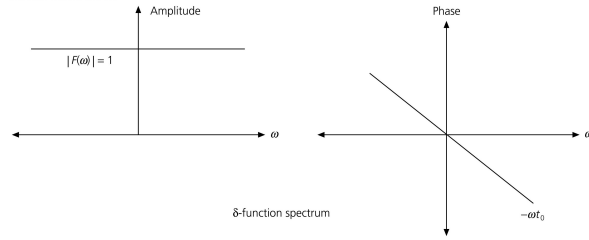
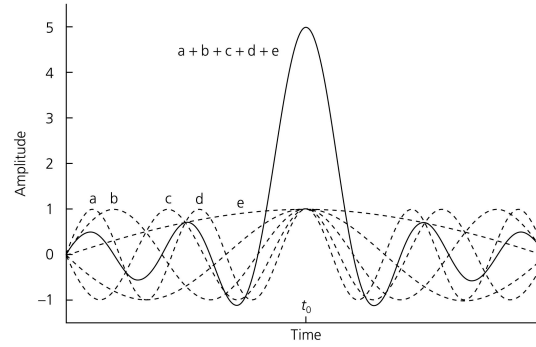
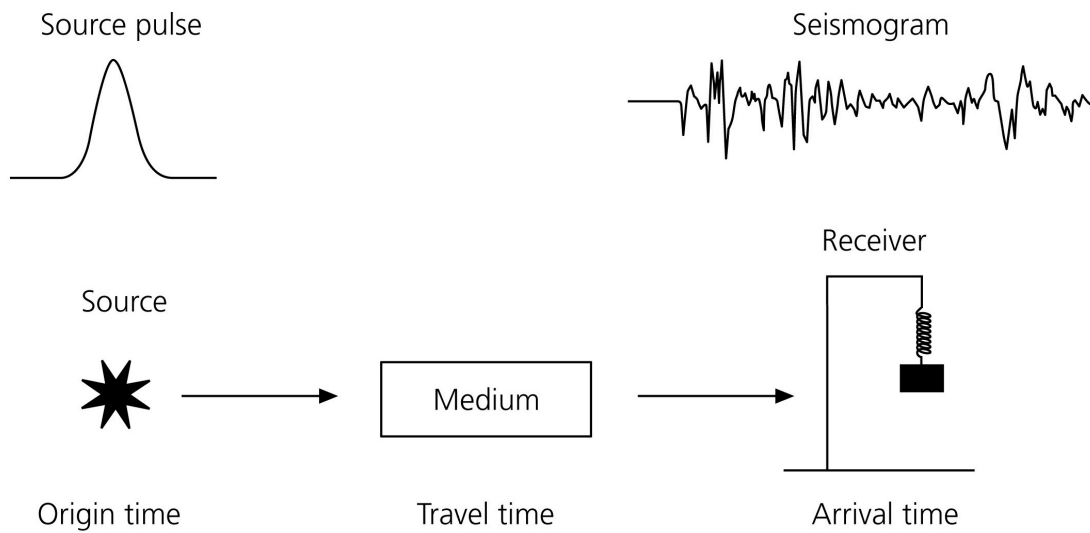


Figure 6.2-7: Fourier transform of a delta function as the sum of sinusoids of all frequencies.



33

Figure 1.1-1: Schematic geometry of a seismic experiment.



34

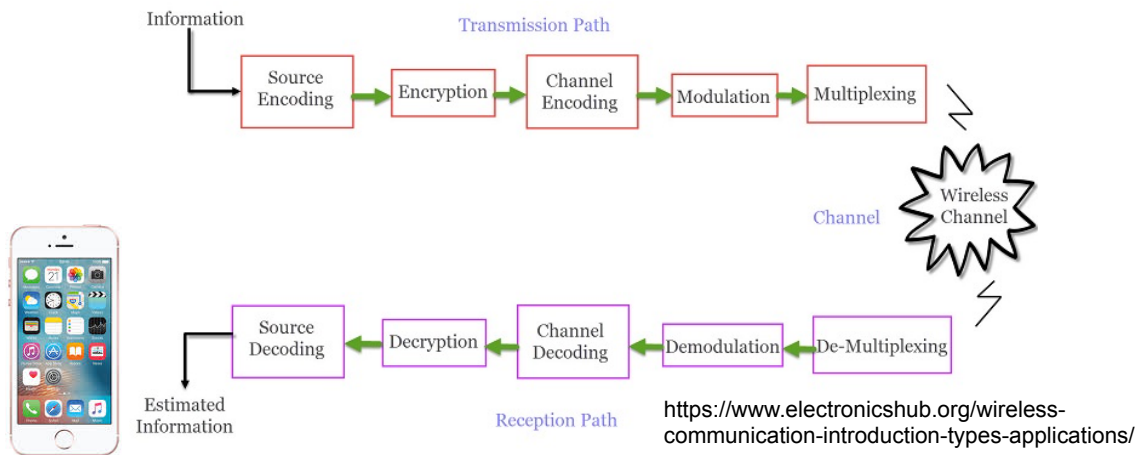
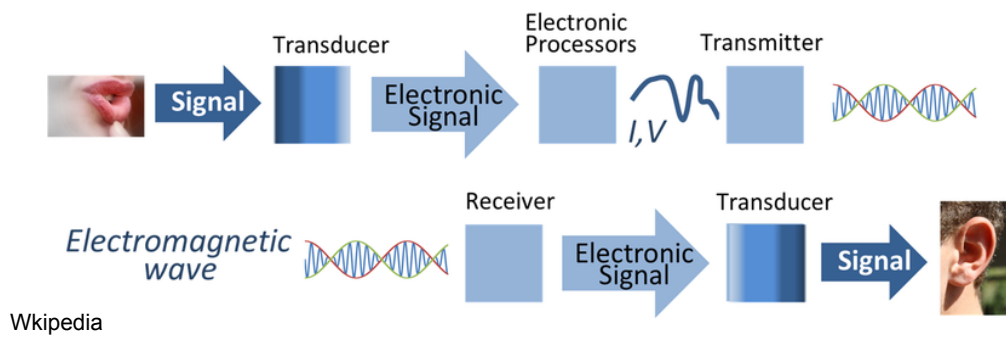


Figure 6.3-1: Definition of a linear system.

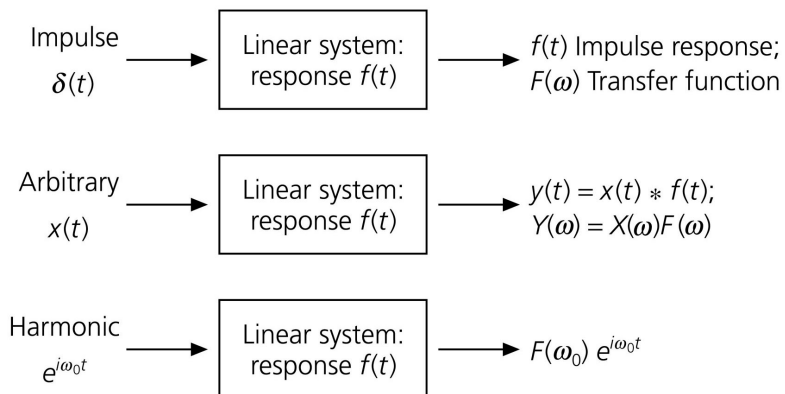
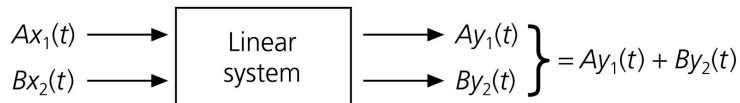


Figure 6.3-4: Two linear systems in succession.

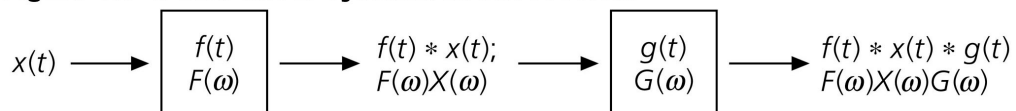


Figure 6.3-3: Bandpass filter in the frequency and time domains.

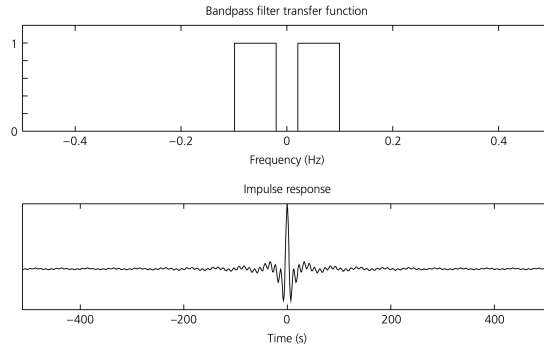


Figure 6.6-11: Use of filtering to enhance different frequency bands of a single seismogram.

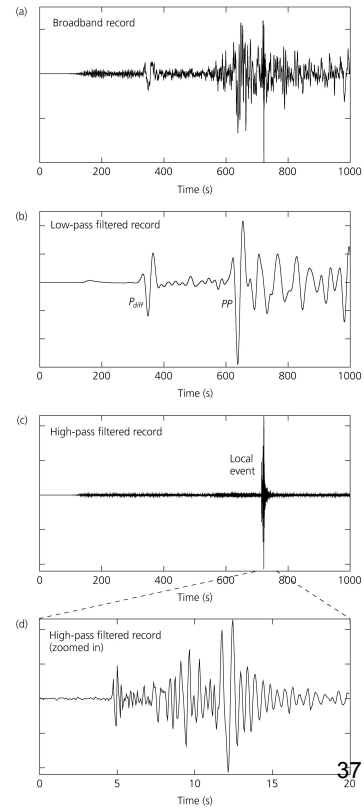
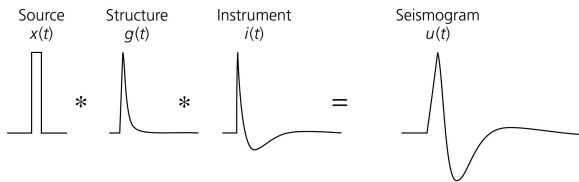


Figure 6.3-5: Seismogram as the convolution of the source, structure, and instrument signals.



Effect of source depth

Figure 4.3-8: Body wave modeling procedure for depth determination.

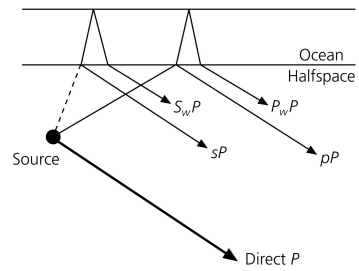
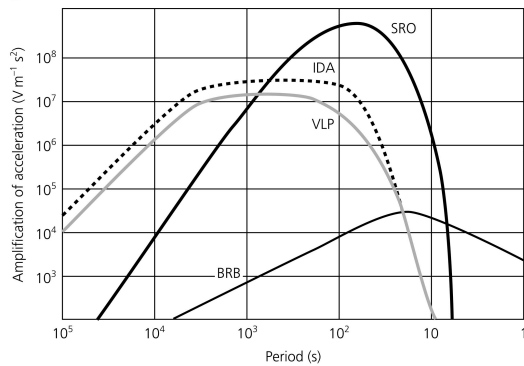


Figure 6.3-6: Transfer functions for various seismometers.



Seismometer is a filter

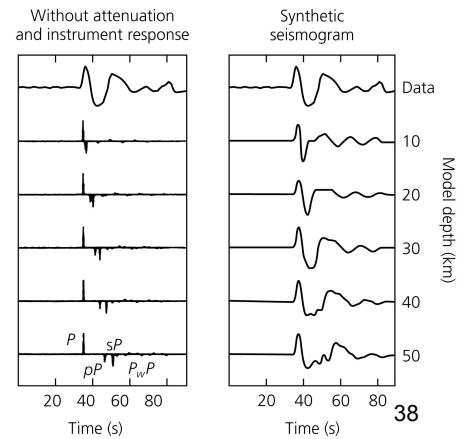
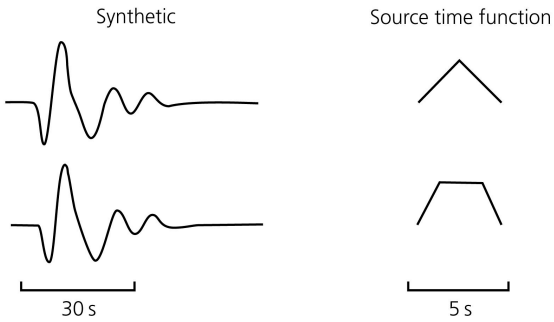
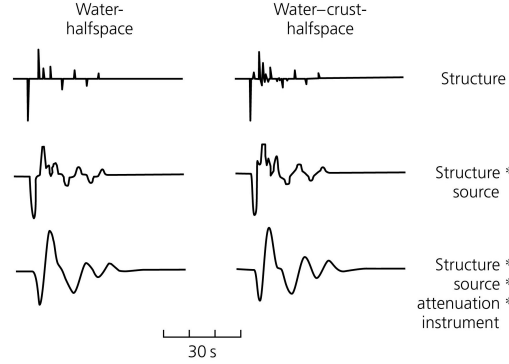


Figure 4.3-10: Effect of source time functions on body waveforms.



Effect of source time function

Figure 4.3-9: Effect of a water layer on body waveforms.



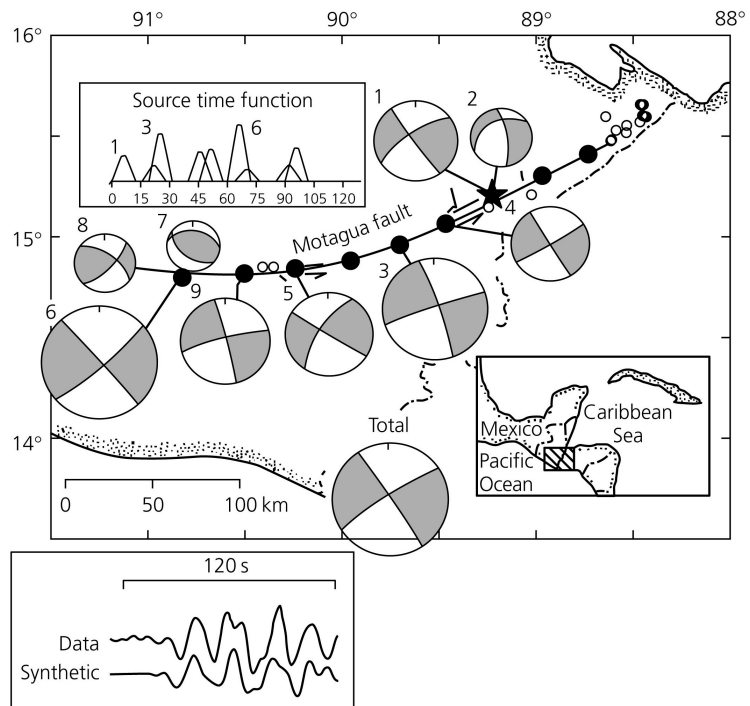
Effect of near-source structure

39

Figure 4.3-11: Example of the determination of a complex rupture for the 1976 Guatemala earthquake.

Large complex earthquakes can be modeled as the sum of source time Green's functions with different amplitudes, C_j , at different times, τ_j :

$$u(t) = \sum_{j=1}^K C_j \left[x(t - \tau_j) * g(t) * i(t) \right]$$



40

Maximum slip ~ 20 m

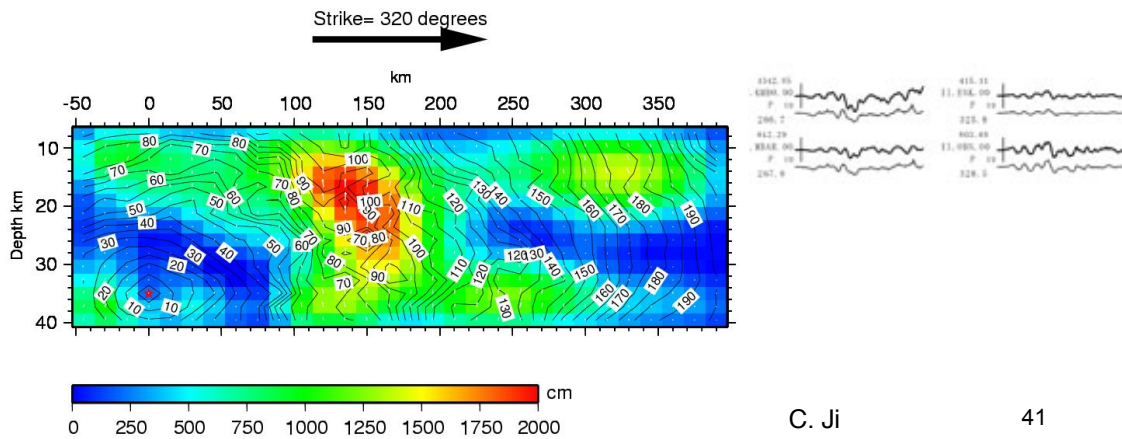
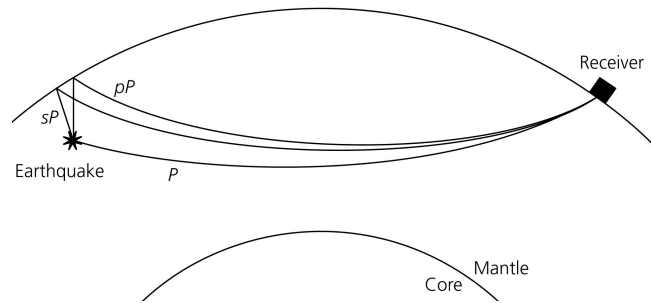


Figure 1.2-3: Estimated earthquake hazards: 2% probability over 50 years.

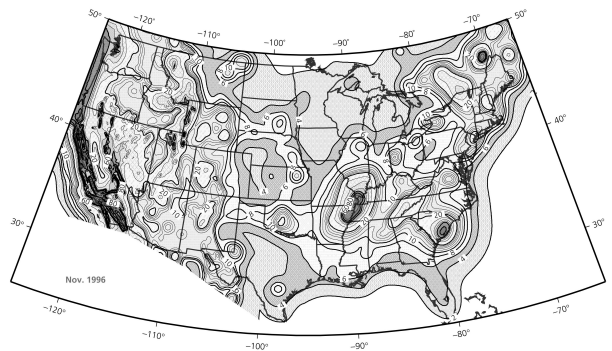


Figure 1.2-5: Predicted strong ground motion in eastern and western U.S.

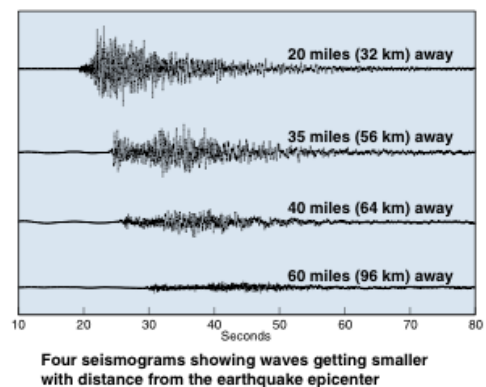
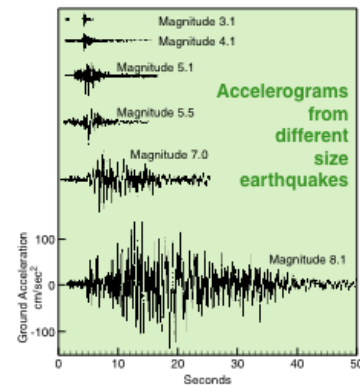
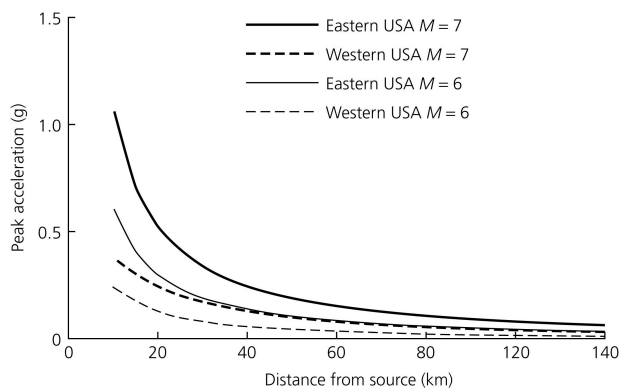
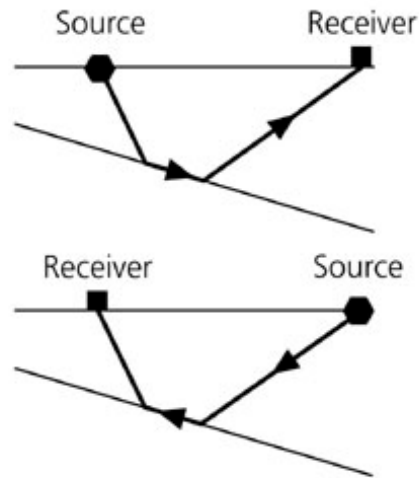




Figure 3.2-12: Difference between



Same travel times
down-dip and up-dip

43

Figure 1.1-5: Demonstration of the seismic reflection method.

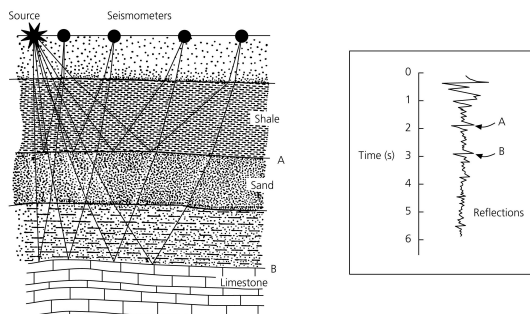


Figure 3.3-28: Reflection seismogram as the convolution of a source pulse with a reflector series.

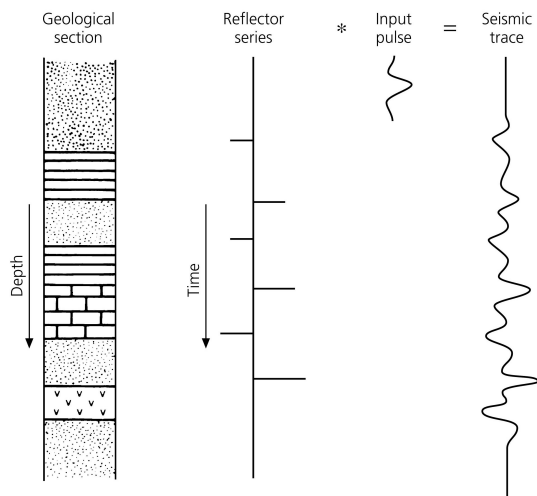
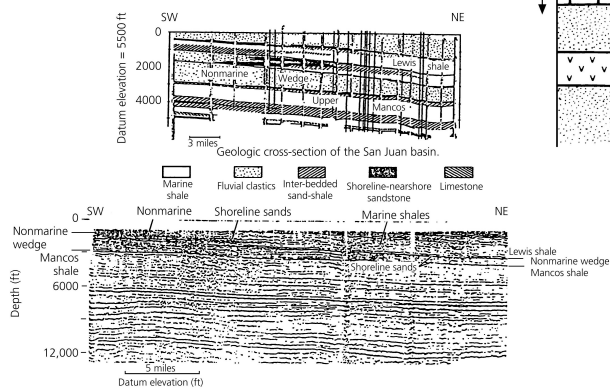
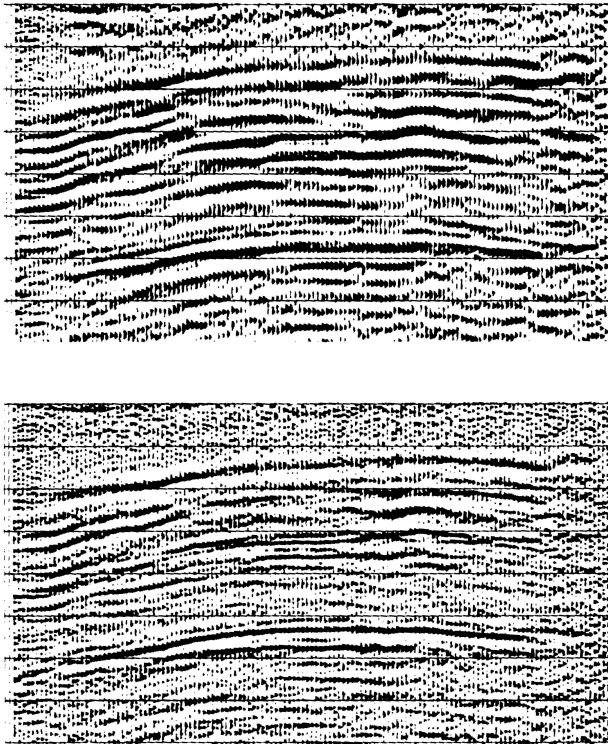


Figure 1.1-6: Example of a seismic reflection survey.



44

Figure 3.3-29: Seismic section before and after deconvolution.



45

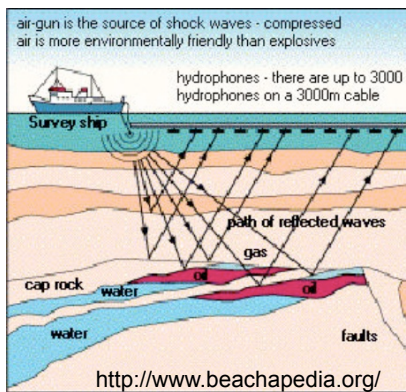
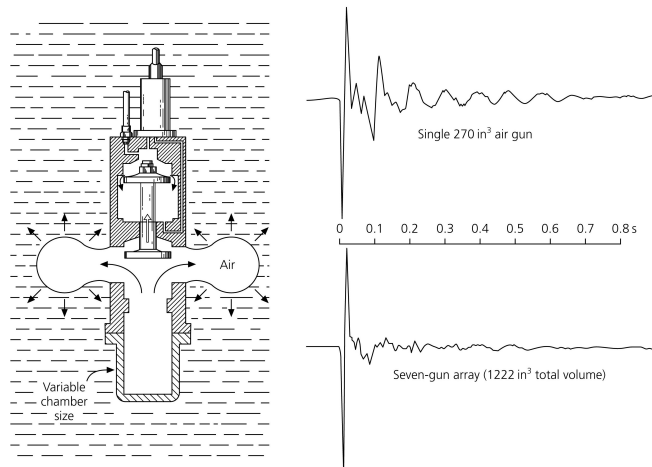


Figure 3.3-25: Illustration of an air gun and its source wavelets.



46

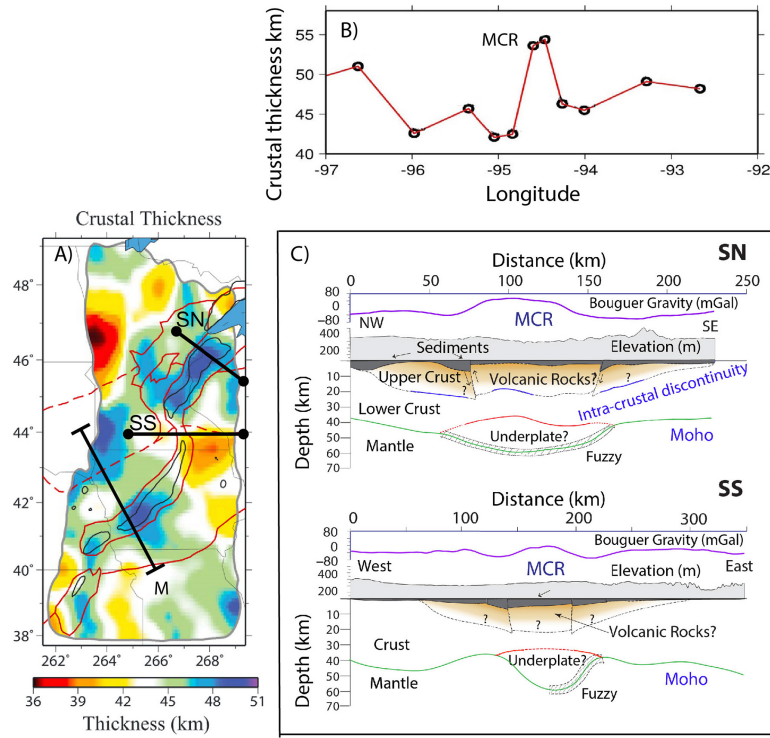
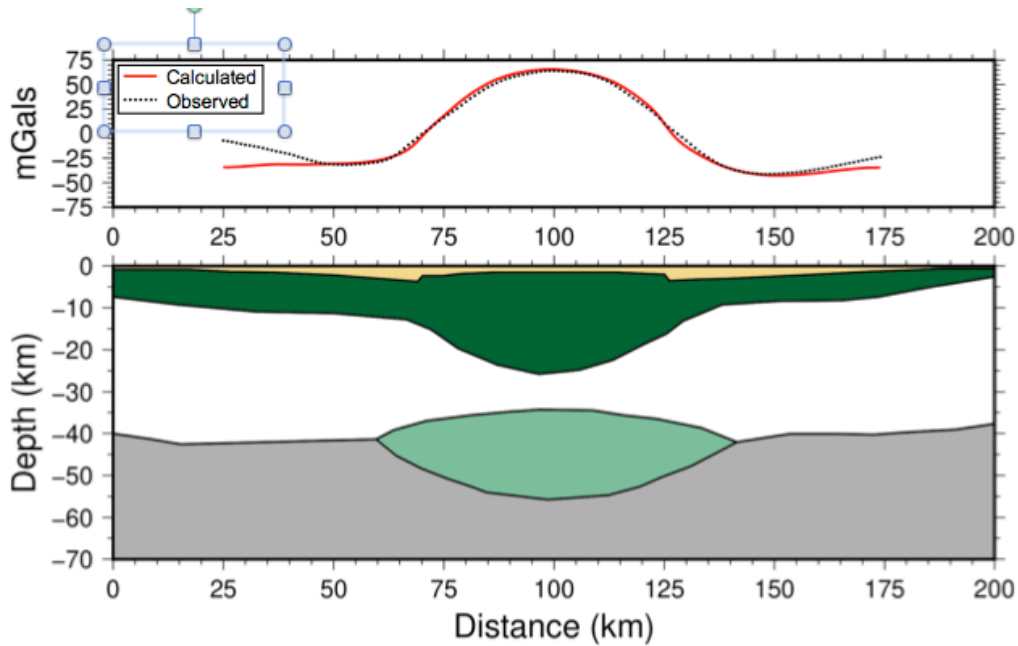


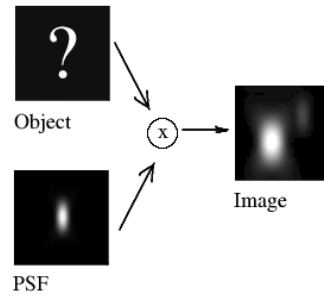
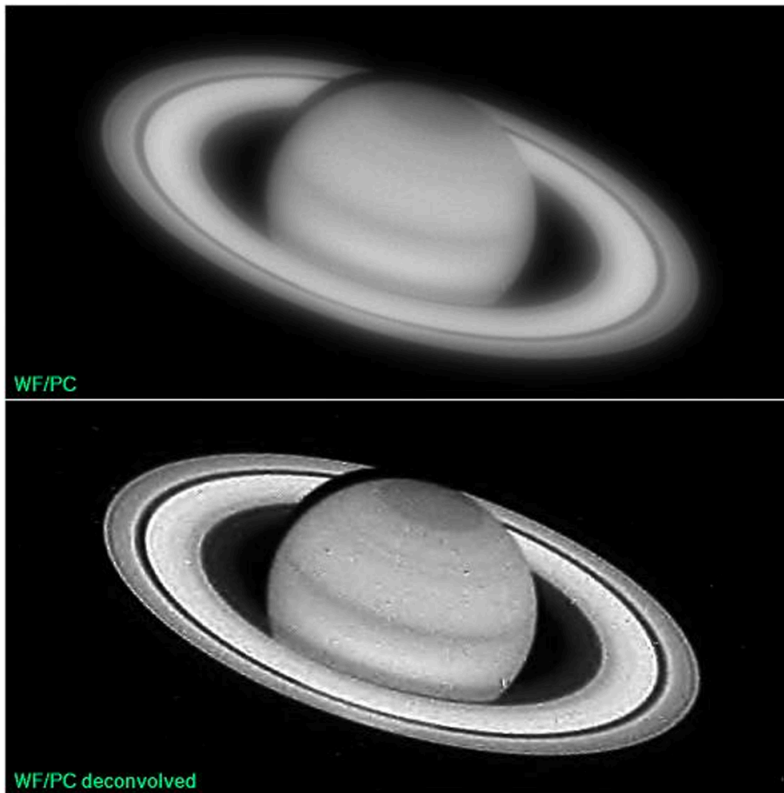
Fig. 12. Crustal thickening beneath the MCR's west arm is shown by surface wave tomography (Shen et al., 2013) (A) and receiver functions (B; Moidaki et al., 2013 and C; after Zhang et al., 2016). Profile locations are indicated in A; M denotes that in panel B) and SS and SN denote those in panel C).

49

MCR West Arm

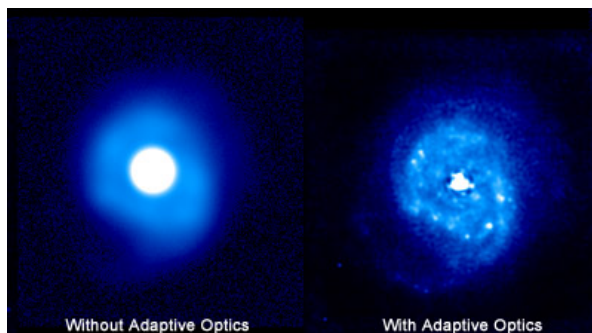


50

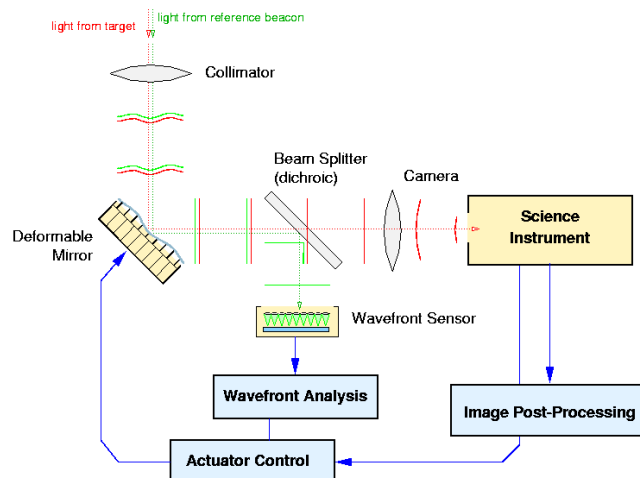


"Experience with the Hubble Space Telescope: 20 years of an archetype"
<http://opticalengineering.spiedigitallibrary.org/article.aspx?articleid=1183218>

51



Adaptive Optics



<http://cfao.ucolick.org/ao/how.php>

Figure 6.3-8: A boxcar function in the time and frequency domains.

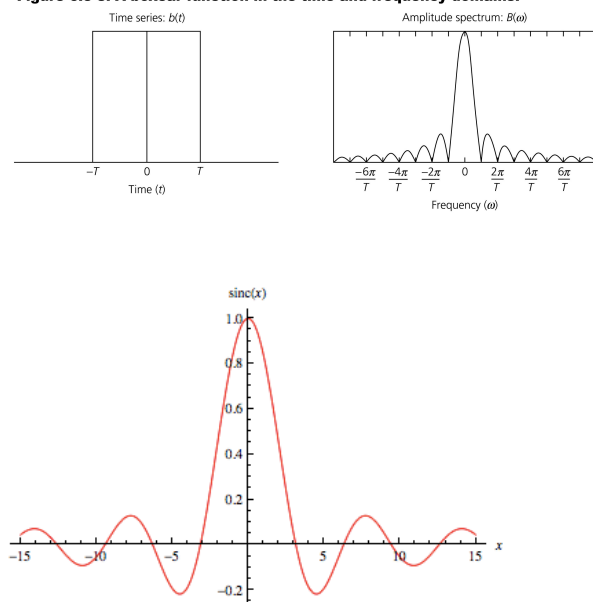
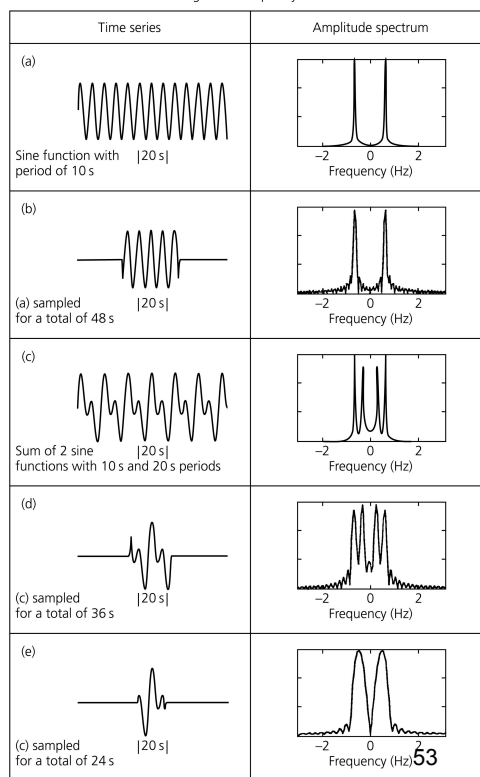
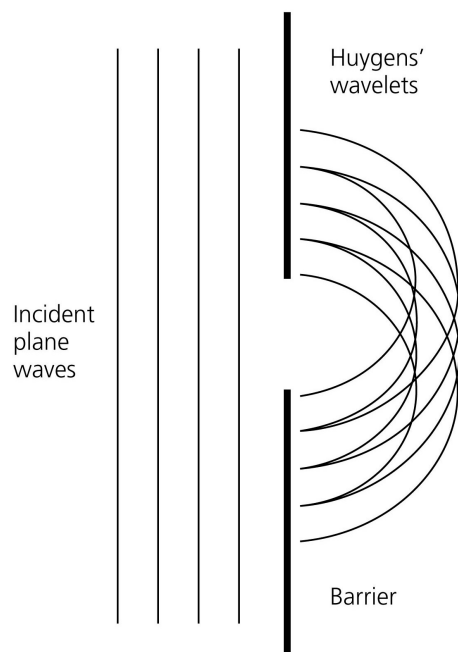
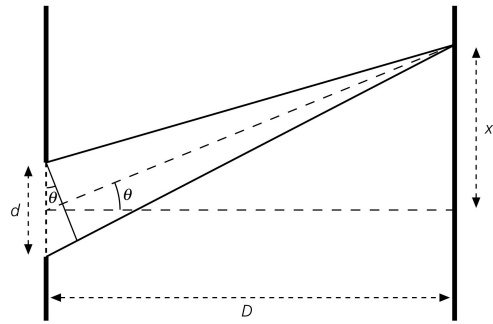


Figure 6.3-9: Effects of windowing time signals on the amplitude spectra.
Data length and frequency resolution



2.5-18: Single-slit diffraction.

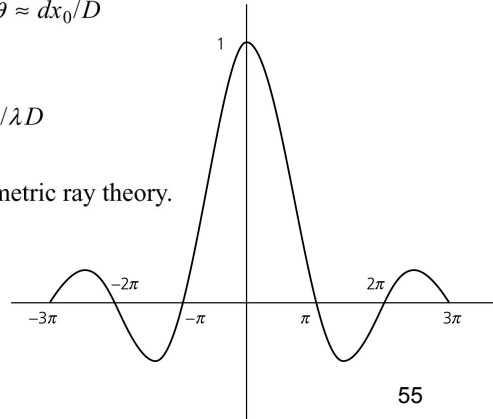




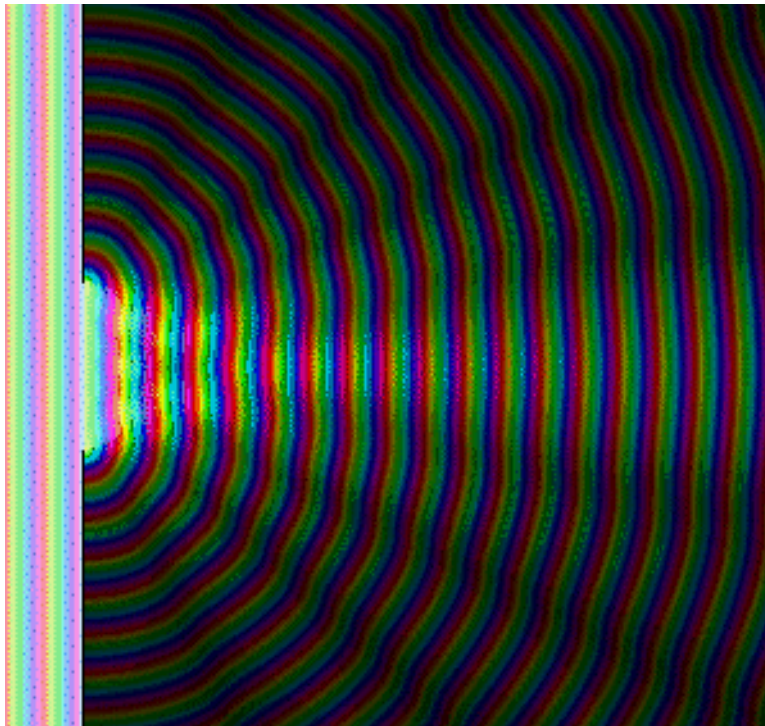
Destructive interference when (for $D \gg d$): $\lambda/2 = d \sin \theta \approx dx_0/D$

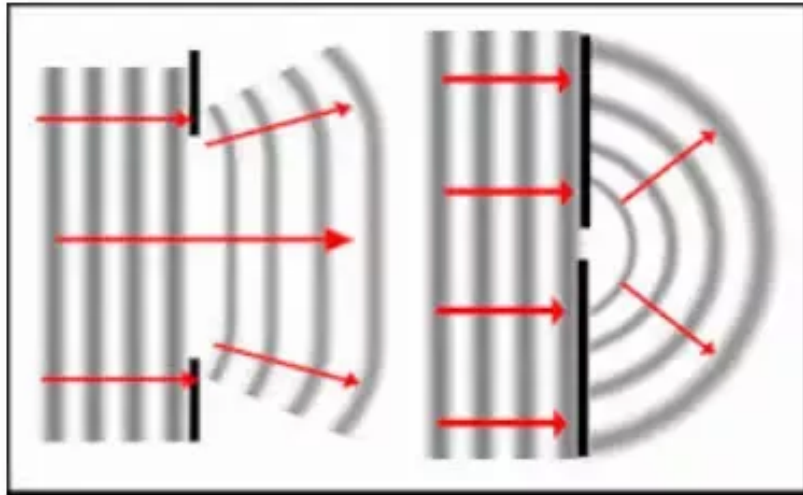
Actual diffraction pattern is: $\frac{\sin \zeta}{\zeta}$ where $\zeta = 2\pi dx/\lambda D$

Diffraction is described by Huygens' principle, but not geometric ray theory.



55





<https://www.quora.com/In-single-slit-diffraction-what-is-the-effect-of-increasing-wavelength-and-the-slit-width>

57

Figure 3.7-11: Wave amplitude for a damped harmonic oscillator.

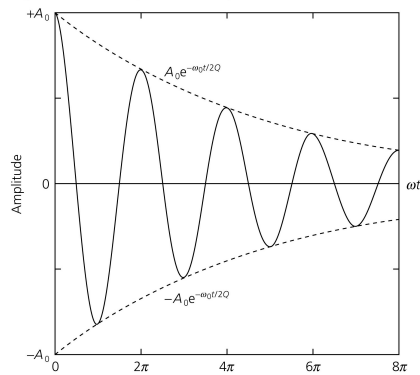
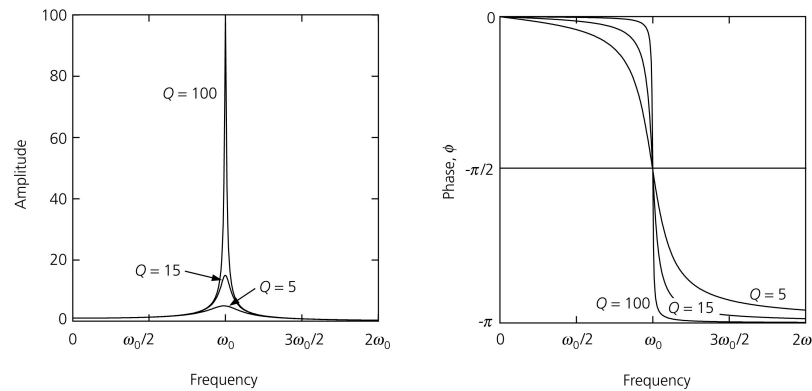


Figure 3.7-13: Amplitude/phase of a forced, damped harmonic oscillator.



58

Figure 2.9-2: Amplitude spectrum shown mode peaks for a 35-hour record.

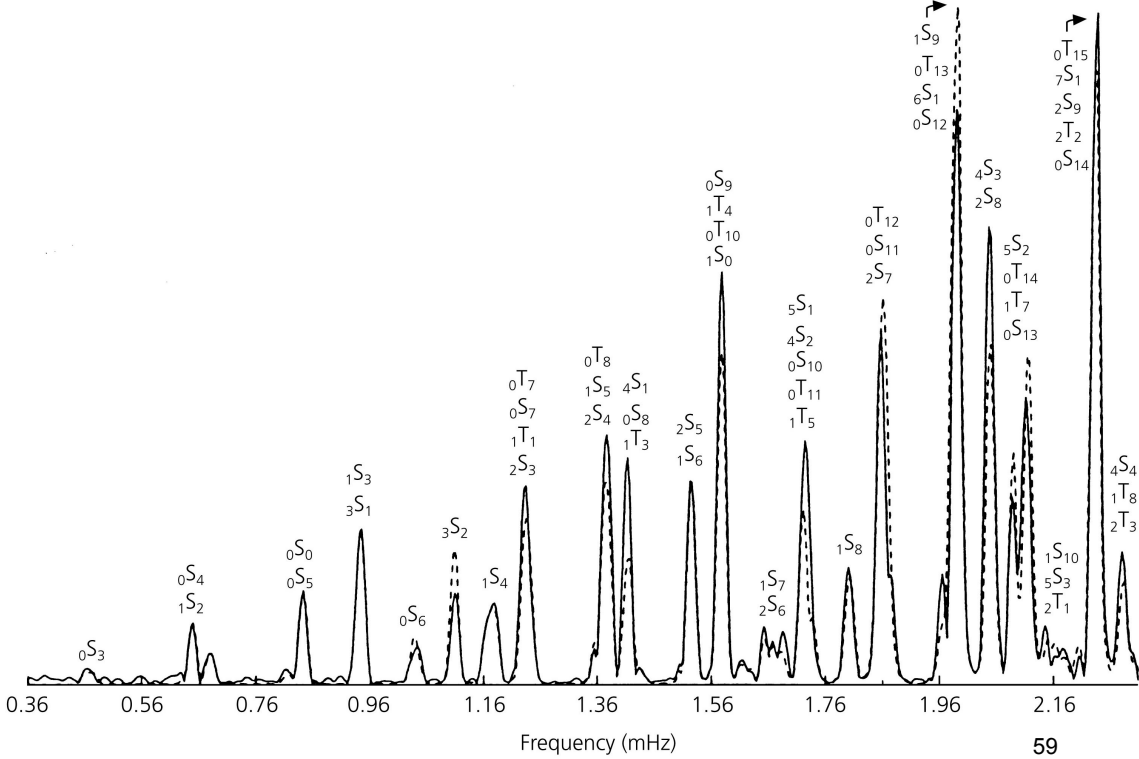


Figure 6.3-10: Effects of tapering a boxcar function on the amplitude spectrum.

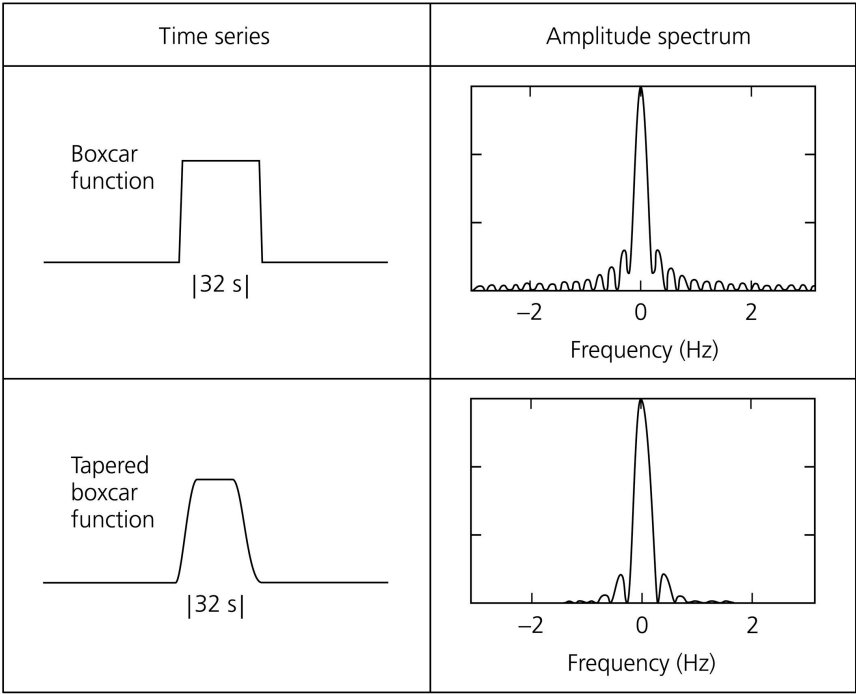


Figure 6.3-11: Using cross-correlation to find a differential SS-S travel time.

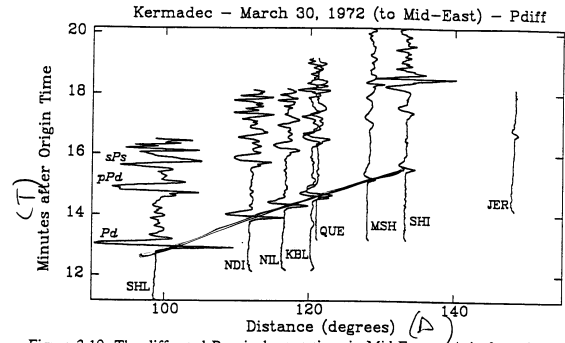
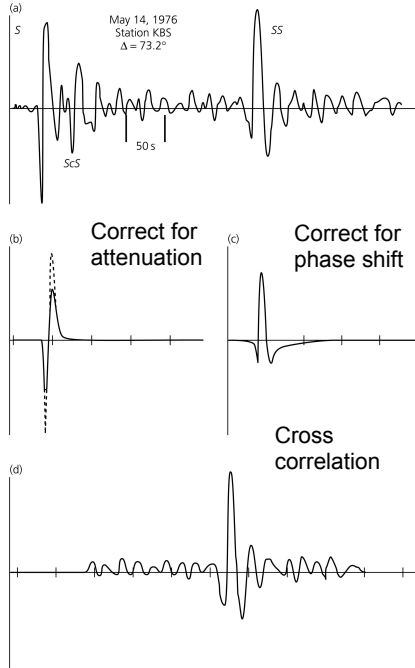


Figure 3.19. The diffracted P arrivals at stations in Mid-Eastern Asia from the earthquake in Kermadec on March 30, 1972.

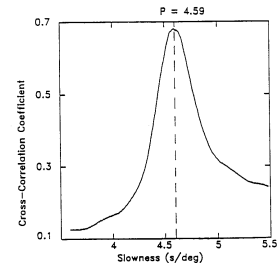


Figure 3.23 An example of the multi-waveform cross-correlation technique used to determine the apparent slowness for profile 12.2 (Kermadec to Mid-Eastern Asia, 3/30/72). The best value of the slowness is the peak of the curve.

Wy session PhD Thesis

$$p = \frac{dT}{dD} = \text{slowness}$$

Figure 3.3-26: Geometry of a Vibroseis survey showing sample signals.

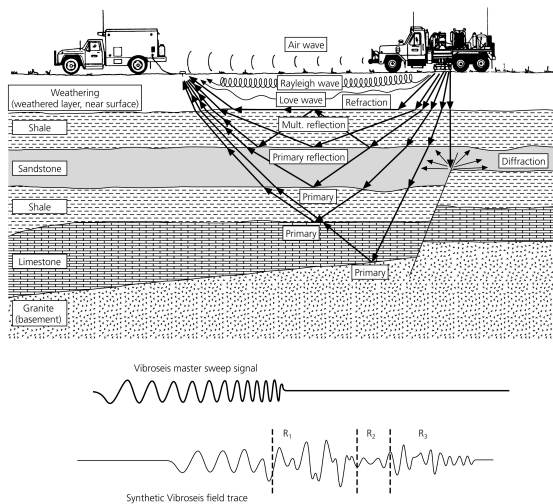


Figure 3.3-30: Auto-correlation of a Vibroseis sweep signal.

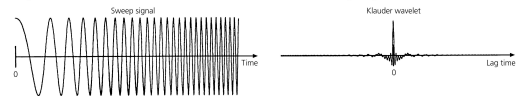


Figure 3.3-31: Analysis of a Vibroseis record.

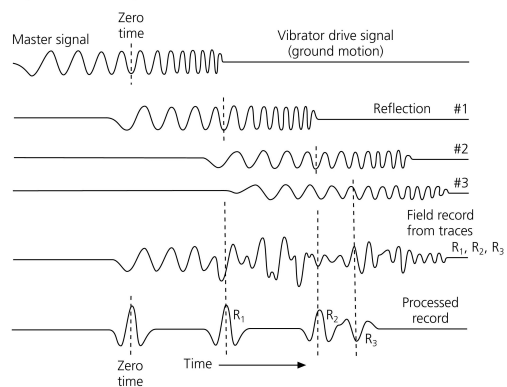


Figure 6.3-12: The auto-correlation is maximum at zero lag and is an even function of the lag.

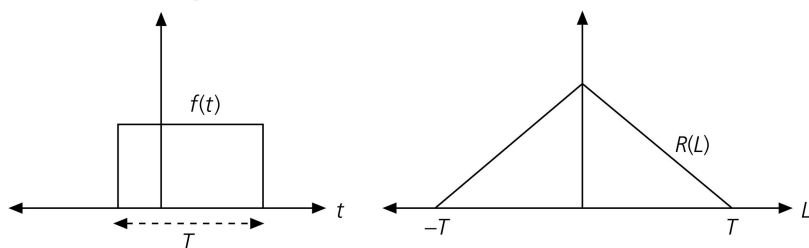
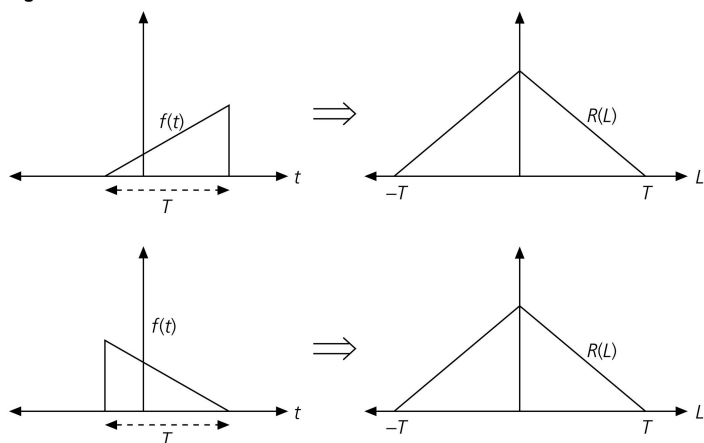


Figure 6.3-13: A function has the same auto-correlation if it is reversed in time.



63

Figure 6.4-1: Use of a Dirac comb in sampling a time signal.

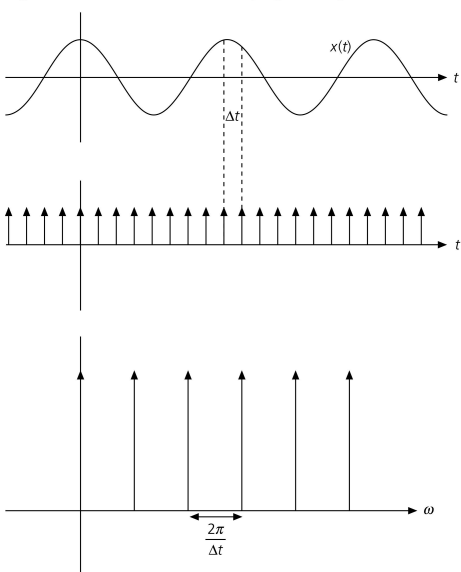


Figure 6.4-2: Effect of sampling a time signal on the frequency amplitude spectrum.

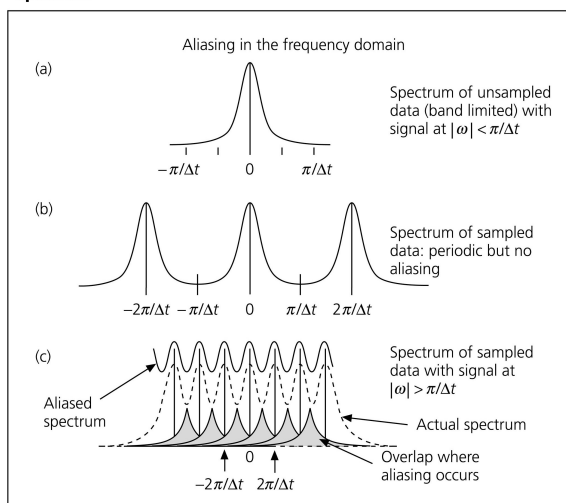
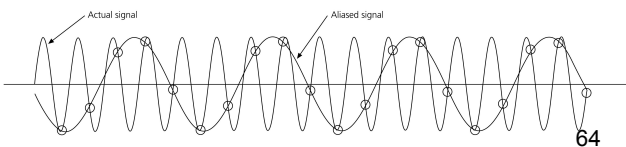
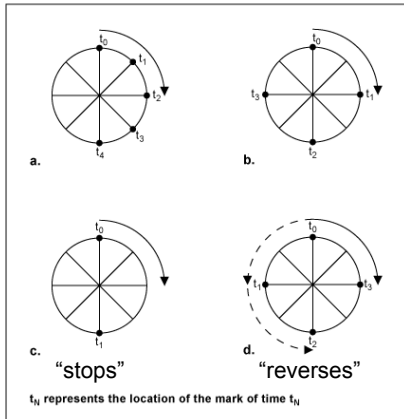


Figure 6.4-3: Example of aliasing in sampling a time signal at less than two samples per wavelength.



64



<https://www.maximintegrated.com/en/app-notes/index.mvp/id/928>

<https://www.youtube.com/watch?v=SFbINinFsxk>

65



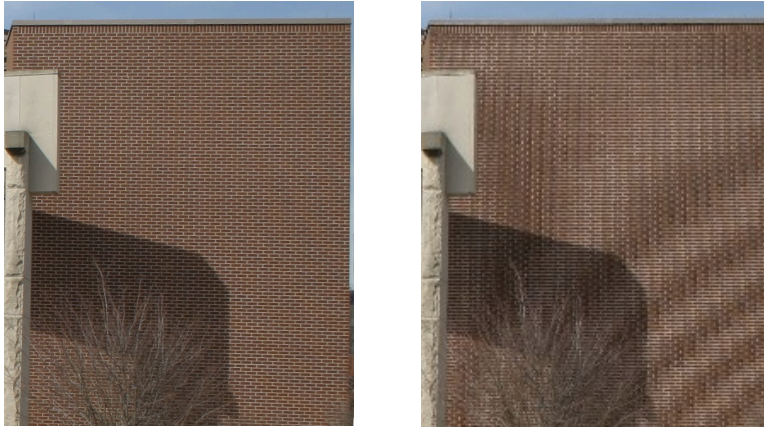
Spatially aliased



With antialiasing
bandpass filter

<http://www.svi.nl/AntiAliasing>

66



<https://en.wikipedia.org/wiki/Aliasing>